University of Alberta

Pressure-driven Liquid Flow in Microchannels

by

Fuzhi Lu 

A thesis submitted to the Faculty of Graduate Studies and Research in partial fulfillment of the requirements for the degree of Master of Science.

Department of Mechanical Engineering

Edmonton, Alberta
Fall 2004

Your file Votre référence
ISBN: 0-612-95805-1
Our file Notre référence
ISBN: 0-612-95805-1

ACKNOWLEDGEMENTS

My acknowledgment list is pretty well endless, but I will try to fit everybody in. I would like to start by thanking my family, my wife Xiaohong Huang, my son Muyu Luhuang. I am fully grateful for what they have done for me in these years.

I would like to acknowledge my advisor, Professor Daniel Y. Kwok, for his patient guidance, continual support and helpful suggestions in my research. I would also like to express my greatest thanks to the Chair of our department, Professor Larry W. Kostiuk, for his suggestion and equipment support. I would like to express my gratitude to the examining committee, Professor Jingli Luo.

Special thanks to all the machinist and technicians: Don Fuhr, Albert Yeun, Dave Pape, Terri Nord, Tulla Hilvo Bernie Faulkner, Andrew Coward and Ian Buttar whose knowledge and abilities helped me a great deal.

Table of Contents

List of Tables

List of Figures

List of Nomenclature

a ..... Half Height or Radius of Channel (m)

c ..... Molar Concentration (mol/m^3)

D ..... Diffusion Coefficient (m^2/s)

e ..... Electron Charge (C)

g_i ..... Gibbs Free Energy (eV)

F ..... Faraday Constant (C/mol)

I_s ..... Streaming Current (A)

I_c ..... Conduction Current (A)

$\vec{i}$ ..... Current Density (A/m^2)

K_b ..... Bulk Conductivity (S/m)

K_σ ..... Surface Conductivity (S)

k ..... Boltzmann Constant (J/K)

L ..... Channel Length (m)

ΔP ..... Pressure Drop Along the Channel (Pa)

R ..... Universal Gas Constant (J/mol K)

R_0 ..... Bulk Electrolyte Resistance (Ω)

R_s ..... Surface Resistance (Ω)

T ..... Temperature (K)

u ..... Velocity Component Along the x Direction (m/s)

v ..... Velocity Component Along the y Direction (m/s)

$\vec{v}$ ..... Velocity (m/s)

W ..... Channel Width (m)

W_{sl} ..... Solid-liquid Adhension Energy (mJ/m^2)

Z_i ..... Valence of Species i

ϵ ..... Permititivity (C/Vm)

κ ..... Inverse of Debye Length (1/m)

μ_i ..... Mobility of Species i (m^2/Vs)

μ_i^0 ..... Chemical Potential (eV)

ρ_e ..... Charge Density (C/m^3)

ρ_d ..... Liquid Density (kg/m^3)

σ_0 ..... Surface Charge Density (C/m^2)

ϕ ..... Electric Potential (V)

ϕ_0 ..... Electric Potential in the Bulk (V)

ψ ..... ϕ-ϕ_0 Potential Relative to the Bulk (V)

ζ ..... Zeta Potential (V)

ν ..... Kinematic Viscosity (m^2/s)

θ ..... Contact Angle

γ_{lv} ..... Liquid-vapor Interfacial Tension (mJ/m^2)

γ_{sv} ..... Solid-vapor Interfacial Tension (mJ/m^2)

γ_{sl} ..... Solid-liquid Interfacial Tension (mJ/m^2)

CHAPTER 1

INTRODUCTION

1.1 Surface effect on microfluidics

Microfluidics is a multi-disciplinary research topic. Many physical and chemical phenomena, which are normally neglected in traditional fluid mechanics, are involved. The most noticeable feature of microfluidics is that chemical and physical properties of surfaces are no longer negligible. Because of the relatively large surface-to-volume and surface-force-to-body-force ratios in micron-scale configurations, surface effects dominate most of the transport phenomena in microchannels [1], which cause apparent differences between microfluidics and macrofluidics. Since traditional hydrodynamic theory cannot predict microfluidic behavior, fundamental understanding including interactions between liquid and solid wall becomes an essential issue. In this thesis, the electrokinetic effects and hydrophobicity effects on liquid flow in microchannels will be studied.

1.2 Electrokinetic flow in microchannels

1.2.1 Electrokinetic phenomena

A potential difference exists at the interface between any pair of conducting phases [2]. The magnitude of the potential is a function of the electrical double layer (EDL) whose structure is determinded by both the composition and nature of the phases. When a solid is dipped into a solution of an electrolyte, the excess charge residing on

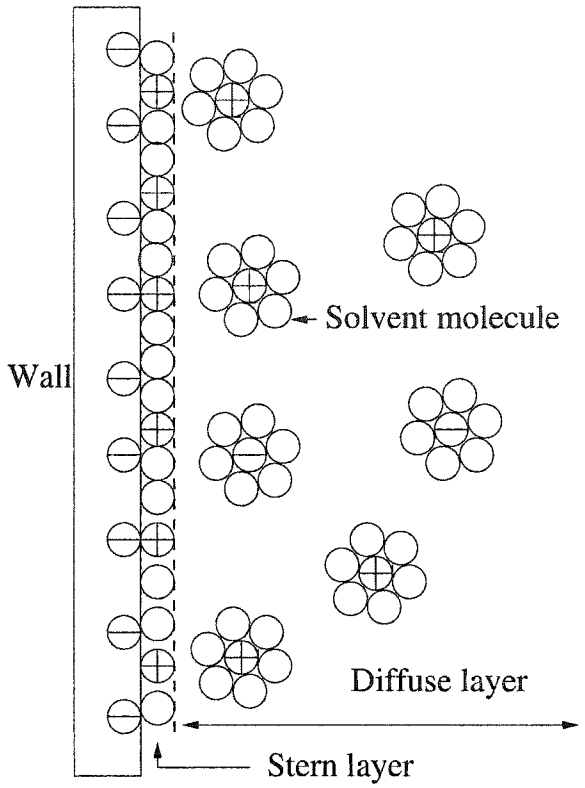

Figure 1.1: Schematic of an electrical double layer at the channel wall

the solid surface must be exactly balanced by an equal charge of opposite sign on the solution side for electroneutrality. The two parts of excess charge which may be ions, electrons or oriented dipoles are called electrical double layer (EDL). Helmholtz [3], who originally formulated the concept of the electric double layer and the equations of electrokinetics, postulated that there is an immobile layer of electric charges of one sign on the solid at solid-liquid interfaces, and a mobile charge of equal magnitude but of opposite sign is arranged in an adjacent layer in the body of the liquid. This concept was developed later by Gouy and Chapman [4, 5]. The widely accepted model for the EDL according to Gouy, Chapman, Stern and Grahame is schematically shown in Fig.1.1 [6]. Because of the electrostatic interaction and thermodynamic motion, the ion (coion and counterion) distribution near the solid surface is different from that in the bulk liquid far away from the surface [7]. Immediately next to the surface, there

is a layer of ions that are strongly attracted to the solid surface and are immobile. This layer is called the compact layer (stern layer), normally less than 1 nm thick. The compact layer is further assumed to be composed of two planes where immobile coions (inner Helmholtz plane) and immobile counterions (outer Helmholtz plane) are adsorbed. From the compact layer to the uniform bulk liquid, the ion concentration gradually changes to that of bulk liquid. This layer is called the diffuse layer of the EDL. The thickness of the diffuse layer depends on the ionic concentration, the ionic valence and the properties of the liquid, ranging from a few nanometers for high concentration solutions up to the order of micrometer for dilute solutions. The thickness of the EDL is usually represented by the Debye-Hückel reciprocal length parameter, κ^{-1}. The boundary between the diffuse layer and the compact layer is for the evaluation of electrokinetic measurement frequently assumed to coincide with the hydrodynamic solid/liquid boundary, usually referred as the shear plane. The electrical potential at shear plane is called zeta (ζ) potential. Zeta potential and κ^{-1} are the two parameters often employed to characterize the EDL.

In addition to ζ and κ^{-1}, another important interfacial electrokinetic parameter is the surface conductance [8]. The surface conductance usually referred to as an excess quantity which occurs, in addition to the liquid bulk conductivity in solid-liquid interfaces, due to charge accumulation in the EDL. It was first suggested by Urban *et al.* [9] that although the outer Helmholtz layer is not displaced by hydrostatic forces, it may nevertheless move in an electric field. Therefore, in many cases, the zeta potential represents only a part of the mobile charge of the double layer, but surface conductance is related to the total mobile charge. A general expression for surface conductivity K_σ on an assumed interfacial plane [10] is

$$K_\sigma = F \sum_i |Z_i| \int_0^\infty [c_i(x) - c_i(\infty)] \mu_i(x) dx \tag{1.1}$$

where F is the Faraday constant, i the index of ith ionic species, Z the valency of the

the ions, c the ion concentrations at the interfacial layer and in the bulk solution, μ_i the mobility of the ions, and x the distance from the surface.

The methods for measuring electrokinetic properties of solid-liquid interface can be classified into one of three categories: electroosmosis, electrophoresis and streaming potential (or streaming current) techniques. In the electroosmotic approach, an electrical potential difference is applied to the ends of a small capillary tube, resulting in a body force applied to the fluid within the double layer region due to the excess charge in the EDL. The body force will push all the liquid in the capillary to flow forward and the measurement of total flow rate can then be related to zeta potential [11]. The limitation of electroosmosis technique is that the accuracy of the measurement is not high enough due to the very low flow rate. In the electrophoresis method [12, 13], the zeta potential is determined by placing fine particles in an electrical field and measuring their mobility. This technique has also been applied to characterize flat surface by initially grinding then into fine particles [14]. However, it is unclear if the surface electrokinetic properties of these particles are equivalent to the pre-crushed surfaces. Likely the most commonly used method of measuring interfacial electrokinetic properties is the streaming potential technique [10, 15, 16, 17]. In the streaming potential technique, a pressure difference is applied across a capillary. When a liquid is forced through the capillary, the charge in the mobile part of the double layer are carried toward one end, resulting in a current flow in the direction of the liquid flow, called the streaming current I_s. The accumulation of charge downstream sets up an electric field [18]. The field causes a current to flow back in the opposite direction, which is called conduction current I_c. The resulting electrostatic potential difference between the ends of the capillary is called the streaming potential. The solid-liquid interfacial electrokinetic properties can be obtained by measuring the electrical current (streaming current mode) or by measuring the electrical potential (streaming potential mode) between two positions up- and down-stream via nonpolarizible electrodes.

The streaming potential must be measured with a very high impedance voltmeter, so that the electric field is not disturbed.

1.2.2 Literature review of electrokinetic flow in microchannels

The phenomenon of streaming potential was discovered by Quinke [19] in 1859. Helmholtz [3] developed the EDL theory in 1879. Gouy [4] in 1910 and Chapman [5] in 1913 independently developed the Helmholtz's EDL theory by introducing the potential and charge distribution in the fluid adjacent to the capillary wall. The potential and charge distribution in EDL was determined by Debye and Hückel [20] by means of a linear Possion-Boltzmann (LPB) equation in 1923. In 1924, Stern [21] improved the theory by introducing an adsorbed layer of counterions (stern layer).

By taking into account the velocity distribution to Helmholtz's EDL theory, Smoluchowski [22] formulated the electrokinetic relationships in 1903. Burgreen and Nakache [23] studied the electrokinetic flow in a very fine parallel-plate slit and derived the streaming potential by employing the complete Navier-Stokes equations in 1964. Rice and Whitehead [24], in 1965, studied theoretically the electrokinetic flow in narrow cylindrical capillaries. Levine *et al.* [25] carried out a semi-analytical extension of Rice and Whitehead's work for high surface potential. Overbeek [26] reviewed the early work in this field and set the classical treatment of electrokinetic processes in capillaries and porous plugs. More recently, Lozada-Cassou [27, 28, 29] improved the Poisson-Boltzmann approach by considering the effect of ionic size, ionic concentration and ionic interaction.

On the experimental side, the effect of electrolyte and solid surface on electrokinetic flow have been reported by many authors [30, 31, 32, 33, 34]. A marked decrease in the streaming potential with decreasing capillary size was first demonstrated by White and Bull *et al.* [16, 35]. This unusual behavior of streaming potential was ascribed to surface conductance [16, 32, 35, 36, 37]. The zeta potential determined

from streaming potential was compared with that from other electrokinetic methods [12, 38, 39, 40, 41]. Since the streaming current method is independent of the conductivity, the streaming current method was employed to determine surface conductance [17, 37, 42]. More recently, the streaming current method was employed to determine the zeta potential of monolayers [43, 44, 45].

A technique employed in the above studies is to assume that the effect of the external field (*i.e.* electric field and flow field) on the ion concentration distributions is small. Accordingly, the ion concentration distributions and other quantities are the same as their static equilibrium values. Recently, the flow field effect on ion concentration distributions was demonstrated numerically by van Theemsche *et al.* and Yang *et al.* [46, 47] in electroosmotic flow. For pressure-driven flow, generally which has a larger Reynolds number, it is expected that flow field has stronger effect on ion concentration distributions. In this thesis, the flow field effect on potential distribution and ion concentration distributions is demonstrated numerically and experimentally.

1.3 The slip of liquid flow in microchannels

1.3.1 Wettability and the slip of liquid flow

Wetting and non-wetting phenomena, the advancing or receding of a liquid at solid-liquid-vapor three phase interface, are common in many natural and industrial processes, such as coating, painting, condensation of stream and cleaning by using detergent. The most direct observation of wettability is to measure contact angles at solid-liquid-vapor interfaces (Figure 1.2). At thermodynamic equilibrium, the relation between the solid-vapor interfacial tension γ_{sv}, the solid-liquid interfacial tension γ_{sl}, the liquid-vapor interfacial tension γ_{lv} and contact angle θ is given by the well-known Young's equation:

$$\gamma_{lv} \cos\theta = \gamma_{sv} - \gamma_{sl} \tag{1.2}$$

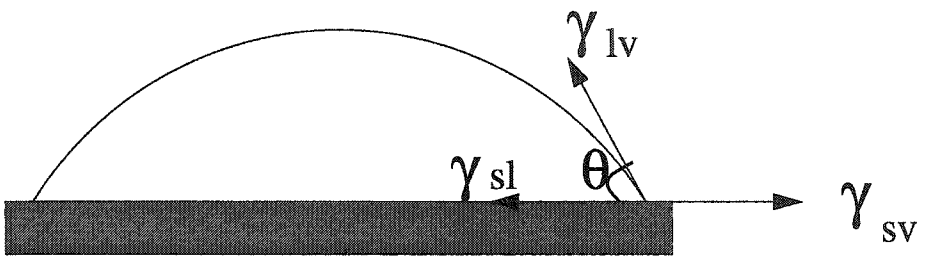

Figure 1.2: Schematic of contact angle phenomena

Thermodynamically, the free energy of adhesion per unit area of a solid-liquid pair W_{sl} can be related to the three interfacial tensions γ_{sv}, γ_{sl} and γ_{lv} by the following equations:

$$W_{sl} = \gamma_{sv} + \gamma_{lv} - \gamma_{sl} \tag{1.3}$$

Eq. (1.3) implies that liquid behavior on a solid surface can reflect the strength of solid-liquid interaction. Water has a relatively large contact angle on a hydrophobic surface and a smaller contact angle on a hydrophilic surface. Therefore, the solid-liquid interaction of water for a hydrophilic surface is stronger than that of a hydrophobic surface.

In contrast with the usual picture where the velocity of a liquid flow on a solid wall is zero, recent experiments [48, 49, 50] have shown that simple liquids may significantly slip on solid surfaces and, consequently, the no-slip condition should be replaced by a more general relation. The following form, first proposed by Navier, is usually adopted

$$\vec{v} = \beta \frac{\partial \vec{v}}{\partial \vec{n}} \tag{1.4}$$

where $\vec{v}$ is velocity vector, β is the slip coefficient (or slip length) and $\vec{n}$ is the unit vector normal to the interface. Experimental results [48, 49, 50] indicate that the slip length is on the order of micrometers, or fractions of micrometers. The main

parameters are the strength of the interactions liquid-solid and the roughness of the substrate. The wettability of liquid on solid surface can reflect the strength of the solid-liquid interactions and the roughness of the substrate.

1.3.2 Literature review of the slip of liquid flow

At a macroscopic scale, the no-slip boundary condition widely used to describe the flow of simple liquids at a solid surface is usually considered very robust. However, it was suggested in early works of Schnell [51] and later by Churaev *et al.* [52] that simple liquids may undergo substantial slip when flowing on non-wetting surfaces. Relying on better experimental conditions numerous recent experiments have directly or indirectly shown that slippage can happen near a hydrophobic microchannel wall even for very low Reynolds numbers. In the case of moderate Reynolds numbers, Watanabe *et al.* [53] observed tap water slippage in a 16 mm diameter acrylic-resin-coated pipe and obtained a 14% drag reduction for Reynolds numbers between 10^2 to 10^3. For Re $\ll 1$, Tretheway and Meinhart [48] measured the velocity profile of water flowing through a 30 $\times$ 300 μm^2 octadecyltrichlorosilane (OTS) coated rectangular microchannel and observed a 1 μm slip length. Zhu and Granick [54] measured the hydrodynamic force of water against a methyl-terminated self-assembled monolayer (SAM) on mica and found that when the flow rate exceeds a critical level, partial slip occurs. It was demonstrated that the classical no-slip boundary condition of fluid flow failed for several systems with hydrophobic surfaces even when the flow velocity is as small as nm/s. It was concluded that the onset of slip varied systematically with contact angle , which depends on the solid surface energy for a given liquid. Cheng and Giordano [55] observed several ten nanometer slippage on photoresist coatings in nanometer-scale channels. Cottin-Bizonne *et al.* [50] used a Dynamic Surface Force Apparatus (DSFA) to measure hydrodynamic force of thin liquid films. Flows of two polar liquids, water and glycerol, on a hydrophilic Pyrex surface and a hydrophobic

octadecyltrichlorosilane (OTS) SAM on Pyrex surface were investigated. No slip boundary conditions were found for both fluids on hydrophilic surfaces. More than one hundred nanometer slip lengths were found on hydrophobic surfaces. Meanwhile, slippage is also found in many molecular dynamic simulations. Thompson and Troian [56] employed molecular dynamics simulations to probe the fluid behavior at the solid-liquid interface and found that surface properties can lead to large fluctuations in the apparent no-slip/slip boundary condition. Molecular dynamic simulations by Barrat and Bocquet [57, 58] of Lennard-Jones liquids have shown that the no slip boundary condition holds on hydrophilic surface.

1.4 Organization of the thesis

In this Chapter, a brief overview of the role of solid-liquid interface interactions in liquid flow has been presented, followed by a detailed and critical review of existing studies related to the present investigation. Chapter 2 demonstrates the effect of flow field on the electrokinetic double layer in parallel-plate microchannels numerically and experimentally. In Chapter 3, the electrokinetic flow with an external load in porous media is investigated. Following the fundamental study on electrokinetic flow in porous media, Chapter 4 describes an electrokinetic (EK) generator. In Chapter 5, a promising slip coating, Self-Assembled Monolayers (SAMs), which are transparent and of a nanoscale thickness, is proposed. Finally, the theoretical and experimental results are summarized in Chapter 6.

Chapter 2

Pressure-driven Electrokinetic Flow in Parallel plate Microchannels

2.1 Introduction

In the past decade, microchannel technology has received attention with major applications in microelectromechanical systems (MEMS) and micrototal analysis systems (μTAS) for chemical and biological analysis. At these micro scales, the surface to volume ratio for fluid flow is large and precise control over mass transfer is essential. A wide range of physical effects that are unimportant for flow at large scale has to be considered and one such effect is the electrokinetic transport phenomena. In pressure-driven flow, the streaming potential will produce an electrical force within the electrical double layer (EDL) which is opposite to the flow direction; this is usually referred to as an electroviscous effect. Thus, the actual flow rate is smaller than that predicted by conventional fluid mechanics theory without consideration of EDL. In electroosmotic flow (EOF) where an external electric field is applied, ion species will be affected by electrophoresis which can be used to produce a separation or mixing of components. Flows that are influenced by these electrical effects are referred to as electrokinetic flow.

The concept of an electric double layer (EDL) and the equations for electrokinetics were originally formulated by Helmholtz. The static EDL theory of Helmholtz [3], which later developed by Gouy [4] and Stern [21], has been employed to streaming

potential studies for decades. The applicability of the static EDL theory to systems composed of solid surface and aqueous solutions of electrolytes has been challenged by experiments using single capillaries as well as porous plugs. It was found that zeta potential values for a given interface calculated from streaming potential measurements do not agree with those from electroosmotic and electrophoretic studies [12, 38, 40, 41, 59]. A variety of experiments, however, showed that zeta potential values for a given interface when calculated from electrophoretic, electroosmotic, and streaming potential measurements can be identical [12, 38, 39].

Another method of testing the static EDL theory as applied to streaming potential is to compare whether or not the zeta potential values determined from streaming potential and streaming current method are identical. It has been found that the absolute values of the apparent zeta potential determined from the latter are generally higher than those from the former [10, 17, 43]. Typically, the zeta potential values from streaming potential are adjusted to be the same as those from streaming current method by varying the surface conductance. Even with this "correction", a small but non-negligible scatter can still be observed in the zeta potential determined for capillaries of different diameters [10]. The difficulty of this approach to test static EDL theory is that surface conductivity cannot be easily measurable since it depends on the size of capillary and the property of an interface. Some authors indeed have employed this method to calculate surface conductivity [17, 42]. The static EDL theory when applied to streaming potential measurements fail to explain the substantial decrease in zeta potential when capillary size decreases and this was first demonstrated by White and Bull *et al.* [16, 35]. By correction through surface conductance, all of these discrepancies appear to be explained satisfactorily. However, as surface conductance is a dependent variable and cannot be measured independently, adjustment of this property in order to compensate for the discrepancy in zeta potential may imply variation of a property that might not truly reflect physical reality. This approach

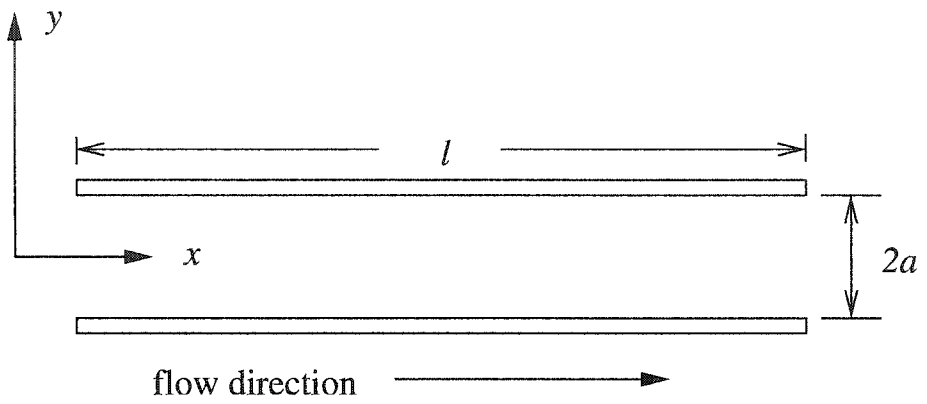

Figure 2.1: Coordinate system for a parallel-plate microchannel system where l and $2a$ are the channel length and height, respectively.

has also been employed to derive surface conductivity [10, 37].

Other than the above experimental approaches, a number of papers have been published recently regarding the various computational methods to electrokinetic flows based on a decoupled approach; i.e., the ion distribution near the EDL is unaffected by its velocity flow field. That is, given the geometry in Figure 2.1, the decoupled approach yields the total potential at a point (x,y) in a channel as

$$\phi = \phi(x, y) = \psi(y) + [\phi_0 - xE_x] \tag{2.1}$$

where $\psi(y)$ is the potential due to double layer at a static state with no fluid motion and no applied external field; ϕ_0 is an imposed potential and E_x is an electric field (assumed to be constant). By superposition of the two potential distributions, Patankar and Hu [60] modeled electroosmotic flow (EOF) in channel junctions using a finite volume approach in three-dimensional channels. Their idea was based on the linearized Poisson-Boltzmann (LPB) equation which can be solved numerically first for the charge distributions along the wall. The external electric field which induces the electric body force can then be obtained by solving a Laplace equation with a properly imposed potential difference. The exact Poisson-Boltzmann (PB) equation

has also been employed by Hu *et al.* [61] based on a similar approach. Ermakov *et al.* [62] hypothesized that the effect of the EDL can be represented by replacing the no-slip condition at the channel wall with an analytical formulation of EOF velocity. A "finite cloud algorithm" method was used by Mitchell *et al.* [63] to compute a steady flow in various channel junctions. A "layer model" was developed by MacInnes [64] for electrokinetic reacting flow where chemical reaction plays a prominent role. However, in geometries where the characteristic dimensions are comparable to the Debye length, these decoupled potential approaches are no longer valid. For this reason, van Theemsche *et al.* and Yang *et al.* [46, 47] proposed a general model which is more valid in such geometries to simulate electrokinetic flow in slit channels. It should be pointed out that this model does not employ the Poisson-Boltzmann equation to govern the electric potential and charge density distribution in EDL. Their numerical simulations, however, are limited to a small length-to-height ratio due to large computational effort. Thus, comparison of such numerical results to experimental data directly is difficult.

In the present work, the effect of flow field on the EDL during streaming potential measurements is studied. The electric potentials in the streamwise direction are measured for pressure-driven liquid flow in a parallel-plate microchannel. By checking their linearity, one may deduce the validity of static EDL theory in streaming potential mode. The electric potential distribution is simulated by numerical solution of the governing equations similar to those by Yang *et al.* and van Theemsche *et al.* [46, 47] but with an assumption of constant liquid conductivity. This assumption allows us to compare the simulated results directly with those from experiments. Instead of the general convection-diffusion-migration equation, a current continuity equation for the distribution of ions is employed here to govern the flux of ion species through the microchannels. The requirement of current continuity has recently been emphasized for heterogeneous microchannels [65]. By solving the established governing equa-

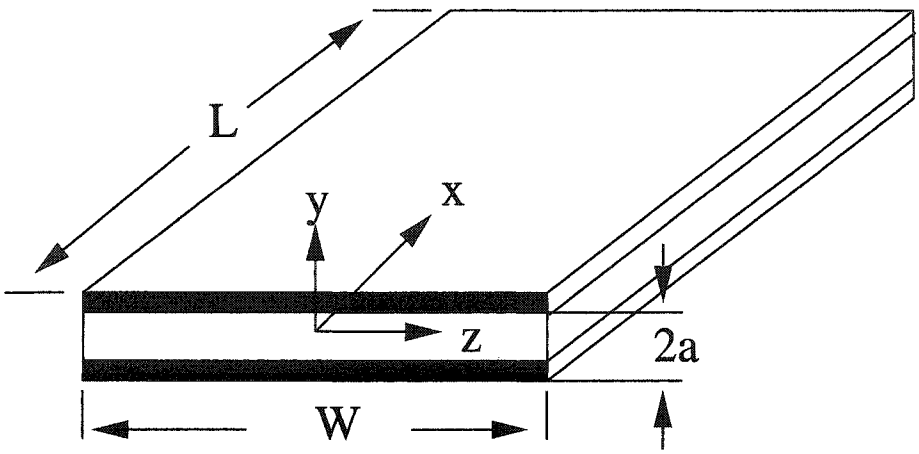

Figure 2.2: Schematic of a parallel-plate microchannel

tions for pressure-driven flow with a finite-volume-based solver in different boundary conditions, the electrical field distribution in EDL is presented and compared with the experimental results. It will be shown experimentally and theoretically that the potential distribution in the EDL along a streamwise direction for a parallel-plate microchannel is non-linear and cannot, in principle, be used for a linear superposition.

2.2 Theory

2.2.1 Classical streaming potential and streaming current measurement with parallel-plate microchannels

A parallel-plate microchannel composed of two flat, parallel, solid surfaces is shown in Figure 2.2. In the cases considered here the height of the channels is much less than their width so that side effects can be ignored and then the channel can be assumed to consist of two parallel surfaces. The fluid flow between two parallel surfaces is well known as the Hagen-Poiseuille or parabolic flow. The velocity profile of the liquid in this case is given by [66]

$$v(y) = \frac{\triangle P}{L}\frac{a^2}{2\eta}(1 - \frac{y^2}{a^2}) \tag{2.2}$$

where y is the variable distance between planes with y=0 at the center-line between the two plates, a is the half height of the channel, L is the length of the channel, η is the dynamic viscosity of the fluid, $\triangle P$ is the pressure drop across the channel and $v(y)$ is the velocity of the liquid which varies only in the y direction in this case. Assuming the thickness of EDL is small enough compared with the channel height, since the excess charge creating the net charge convection in the fluid flow is located in a thin region near the surface, the velocity profile can be further simplified,

$$v(y) \simeq \frac{\triangle P}{L}\frac{a^2}{2\eta}(1-\frac{y}{a}) \tag{2.3}$$

The streaming current created by the flow of the electrical charge in the mobile double layer is given according to

$$I_s = 2\int_0^a v(y)\rho_e(y)Wdy \tag{2.4}$$

where W is the width of the channel and $\rho_e(y)$ the net charge density across the channel. The distribution of charge density is described by the Poisson equation, which for the case being considered here is used to express $\rho_e(y)$,

$$\rho_e(y) = -\varepsilon_o\varepsilon_r\frac{d^2\psi}{dy^2} \tag{2.5}$$

where ε_o is the electrical permittivity of a vacuum, ε_r is the relative dielectric constant of the liquid, and ψ is the electrical potential at any position y. With equations (2.3), (2.4), and (2.5) , the streaming current I_s may be written as

$$I_s = -\frac{2\triangle p\varepsilon_o\varepsilon_r Wa}{\eta L}\int_{y=0}^{y=a} ydy\frac{d^2\psi}{dy^2} \tag{2.6}$$

Assuming that ψ and $d\psi/dy$ at y=0 become zero and $\psi(y = \pm a) = \zeta$, through integration by parts of eq. (2.6) one obtains,

$$I_s = -\frac{2\triangle p\varepsilon_o\varepsilon_r Wa\zeta}{\eta L} \tag{2.7}$$

Solving Eq. (2.7) for ζ gives

$$\zeta = -\frac{\eta}{\varepsilon_o \varepsilon_r} \frac{I_s}{\triangle P} \frac{L}{2Wa} \tag{2.8}$$

The conduction current can be related with streaming potential U_s according to Ohm's law,

$$I_c = \frac{2aWU_sK_b}{L} + \frac{2WU_sK_\sigma}{L} \tag{2.9}$$

where K_b is bulk conductivity. Assuming the streaming current is equilibrated solely by conduction current, the equilibrium state can be obtained by zero net current.

$$I_s + I_c = 0 \tag{2.10}$$

Inserting Eqs. (2.7) and (2.9) into this condition yields the following expression,

$$\frac{2aWU_sK_b}{L} + \frac{2WU_sK_\sigma}{L} = \frac{2\triangle p \varepsilon_o \varepsilon_r Wa\zeta}{\eta L} \tag{2.11}$$

Solving Eq. (2.11) for ζ gives

$$\zeta = \frac{\eta}{\varepsilon_o \varepsilon_r} \frac{U_s}{\triangle p} (K_b + \frac{K_\sigma}{a}) \tag{2.12}$$

Equations (2.8) and (2.12), or some variations thereof, are the bases for the evaluation of the electrokinetic properties of a solid-liquid interface from streaming current and streaming potential measurements.

The derivation of Eq. (2.8) assumes a thin EDL and that of Eq. (2.12) assumes that the conduction current in streamwise direction is the only current to equilibrate the streaming current.

2.2.2 The potential distribution for pressure-driven flow

Helmholtz [3] assumed that there is an immobile layer of electric charges on a solid at the solid-liquid interface, and another mobile layer of opposite charges in the liquid.

If the solid is held in position while the liquid passes through, the movement of liquid will cause a potential gradient in the streaming direction which is known as the streaming potential gradient. The total potential, that builds up in the direction of streaming in this manner, is the streaming potential. It was later realized that the solution layer must be diffused; the charge and electrical potential distributions can be obtained by solving the Poisson-Boltzmann equation. Based on the theory of Helmholtz, the streaming current I_s created by continual transfer of electricity as liquid flows will be balanced by a back current I_c caused by the streaming potential and liquid conductivity. As pointed out earlier,the equilibrium state is characterized by a zero net current Eq. (2.10) through the channel [67]. Equation (2.10) implies that both I_s and I_c are in the streamwise direction and Boltzmann distribution remains valid with the introduction of a flow field. In other words, the conduction current in the y direction is assumed to equilibrate exactly by the diffusion current in the same direction. In fact, the Boltzmann distribution can be derived from the balance between diffusion and conduction currents [64]. Assuming the specific conductivity of liquid and surface to be constant in the streaming direction, and if there is no path other than that through the liquid and the surface by which I_c may pass, the electric potential distribution along the streamwise direction should be linear as given by Ohm's law. The total potential at a point (x,y) in Figure 2.1 will be a superposition of EDL and streaming potentials. If the difference between surface potential and zeta potential ζ is neglected, the measured electric potentials $\phi_{sf}(x)$ near the solid-liquid interface are the superposition of the potential in the bulk $\phi_B(x)$ and zeta potential ζ given by

$$\phi_{sf}(x) = \phi_B(x) + \zeta = -\frac{I_c}{K_b + K_s}x + \zeta = \frac{\phi_s}{l}x + \zeta \tag{2.13}$$

where K_b and K_s are the specific conductivity of the bulk liquid and surface, respectively; ϕ_s is the streaming potential across the two ends with a channel length l.

According to Eq. (2.13), the potential distribution in the streaming direction will be linear with a constant electric field E_x ($E_x = \phi_s/l$).

2.2.3 Electrokinetic equations

The electric field in a dielectric carrying free charge is governed by the Poisson equation. It is assumed that magnetic field, either applied or induced by current flow, may be neglected. The Poisson equation is given by

$$\nabla(\epsilon\nabla\phi) = -\rho_e \tag{2.14}$$

where ρ_e is the net charge density, ϵ is the permittivity of the medium, and ϕ is electric potential. The net charge density can be expressed in terms of species molar concentration c_i as

$$\rho_e = F\sum_i Z_i c_i \tag{2.15}$$

where F is the Faraday constant, Z_i is the valence of species i. Assuming that the flow is dominated by the solvent, the flux $\vec{j_i}$ of species i is given by Nernst-Planck equation.

$$\vec{j_i} = c_i\vec{v} - D_i\nabla c_i - Z_i\mu_i F c_i\nabla\phi \tag{2.16}$$

where $\vec{v}$ is the fluid velocity, D_i represents the diffusivity and μ_i is the ion-mobility. Equation (2.16) expresses the flux of each species i in the solution due to convection of the solvent, diffusion and migration. If the ith species does not carry an electric charge, Eq. (2.16) still hold while setting Z_i to zero. The general convection-diffusion-migration equation with chemical reaction is given by [64]:

$$\frac{\partial c_i}{\partial t} = -R_i - \nabla\cdot(\vec{v}c_i) + Z_i\mu_i F\nabla\cdot(c_i\nabla\phi) + D_i\nabla^2 c_i \tag{2.17}$$

where R_i is the reaction rate. In addition to viscous and pressure stresses, the species in the liquid and the liquid itself are subjected to an electric force. Together with

the mass continuity equation, the pressure and velocity field can be described by the following incompressible Navier-Stokes equations

$$\frac{\partial \rho \vec{v}}{\partial t} + (\rho \vec{v} \nabla) \cdot \vec{v} = -\nabla p - \rho_e \nabla \phi + \nabla(\mu \nabla) \cdot \vec{v} \tag{2.18}$$

$$\nabla \cdot \vec{v} = 0 \tag{2.19}$$

where p is pressure, ρ the density and μ the viscosity of the liquid. The liquid density has been assumed to be uniform as the variation of liquid density caused by the difference in pressure and temperature is negligible. If charge is transferred in the liquid only by movement of ions, the charge distribution is determined by solving the species transport equation (2.17). The summation over all species of the product of species charge gives the charge continuity equation

$$\frac{\partial \rho_e}{\partial t} + \nabla \cdot \vec{i} = 0 \tag{2.20}$$

where $\vec{i}$ is the electric current flux given by

$$\vec{i} = \sum_i Z_i F(-D_i \nabla c_i + \vec{v} c_i - \frac{Z_i F D_i c_i}{RT} \nabla \phi) \tag{2.21}$$

For electroneutral and uniform solutions, the first two terms on the right-hand side vanish. In this case, Ohm's law between current flux and potential gradient applies

$$\vec{i} = -\sum_i \frac{Z_i^2 F^2 D_i c_i}{RT} \nabla \phi = -\sigma \nabla \phi \tag{2.22}$$

where σ is the conductivity of the solution defined as

$$\sigma = \sum_i \frac{Z_i^2 F^2 D_i c_i}{RT} \tag{2.23}$$

For the case of equal species diffusivity $D_i = D$, Eq. (2.21) can be written as

$$\vec{i} = -D \nabla \rho_e - \sigma \nabla \phi + \rho_e \vec{v} \tag{2.24}$$

One can see from this relation that the current flux arises from three mechanisms: (1) diffusion current when spatial variation of charge density is present, (2) conduction current depending on the conductivity of the liquid and the presence of an electric field, (3) convection current caused by the flow which depends on the liquid having a net charge density. At steady state, the current continuity equation is given by that the divergence of current flux equals zero.

$$\nabla \cdot \vec{i} = -D\nabla^2 \rho_e - \nabla \cdot (\sigma \nabla \phi) + \nabla \cdot (\rho_e \vec{v}) = 0 \tag{2.25}$$

By solving the set of equations (2.14), (2.17), (2.18) and (2.19) simultaneously with the appropriate boundary conditions, one obtains the distribution of $\vec{v}$, ϕ and c_i. The equations presented are first applied to some simplified cases in a review of classical results. The assumptions in deriving the classical streaming potential equations are then analyzed.

2.2.4 Boltzmann distribution near a charged surface

2.2.4.1 Heuristic Method

Consider a charged flat surface whose normal is in the y-direction.The local electrochemical potential of an ion at a distance y from an infinitely charged surface is

$$g_i = \mu_i^0 + kT \ln N_i + Z_i e \ \phi \tag{2.26}$$

where g_i is Gibbs free energy, μ_i^0 is the pure chemical potential component, k is the Boltzmann constant, T is the absolute temperature, N_i is number concentration, ϕ is the electrical potential. As the system is electrically neutral, the charge conservation law gives

$$\sigma_0 + \sum_i Z_i N_i = 0 \tag{2.27}$$

where σ_0 is the surface charge density. At equilibrium, the gradient of the electrochemical potential will be zero, implying that

$$\nabla g_i = 0 \tag{2.28}$$

This equation can be solved to give the well-known Boltzmann distribution

$$N_i = N_{i0} \exp(-\frac{Z_i e\phi}{kT}) \tag{2.29}$$

or

$$c_i = c_{i0} \exp(-\frac{Z_i F\phi}{RT}) \tag{2.30}$$

where N_{i0} and c_{i0} are the number and molar concentration of species i respectively as $y \rightarrow \infty$.

2.2.4.2 Nernst-Planck method

The Boltzmann distribution was previously derived using heuristic arguments. It can also be derived by employing the Nernst-Planck relationship. Consider the same system as before, the mass conservation of species i is described as a balance between diffusion flux and electrical migration flux:

$$Z_i \mu_i F c_i \nabla\phi + D_i \nabla c_i = 0 \tag{2.31}$$

The solution of this equation with $c_i = c_{i0}$ at $\phi = \phi_0$ gives

$$c_i = c_{i0} \exp(-\frac{Z_i F(\phi - \phi_0)}{RT}) \tag{2.32}$$

For $\phi_0 = 0$, the Boltzmann distribution shown in Eq. (2.30) is obtained. It should be realized that the Nernst-Planck relationship yields the Boltzmann distribution with the explicit assumptions of that diffusion flux equals to migration flux. In a flow system the above assumpsions may not be true.

2.2.4.3 The Solution of Possion-Boltzmann Equation

Taking liquid permittivity as a constant and substituting the Boltzmann relation into the Poisson equation gives the Poisson-Boltzmann equation

$$\nabla^2\phi = -\frac{F}{\epsilon}\sum_i Z_i c_{i0} e^{(-Z_i F\phi/RT)} \tag{2.33}$$

when the boundary conditions $\phi = \zeta$ (assuming the potential at the surface is zeta potential) at y=0 and ϕ=0 as $y \to \infty$ are applied and the solution for a 1:1 electrolyte is

$$\tanh\frac{F\phi}{4RT} = \tanh[\frac{F\zeta}{4RT}]e^{-\kappa y} \tag{2.34}$$

where y is the distance from the wall position and κ^{-1} which takes the form $\kappa^2 = \frac{\sum_i Z_i^2 F^2 c_{i0}}{\epsilon RT}$ is the Debye length. The zeta potential ζ is given by [68],

$$\zeta = \frac{2RT}{F}\ln(s/2 + \sqrt{1 + s^2/4}) \tag{2.35}$$

where s is a dimensionless surface charge

$$s = \frac{F}{\epsilon RT\kappa}\sigma_0 \tag{2.36}$$

When the value of zeta potential is small, say, $|\zeta| \leq 25$ mV, the Debye-Hückel approximation may be used and the linearized Poisson-Boltzmann (LPB) equation is given by

$$\nabla^2\phi = \kappa^2\phi \tag{2.37}$$

The solution of LPB equation is

$$\phi = \zeta e^{-\kappa y} \tag{2.38}$$

where ζ is given by

$$\zeta = \frac{\sigma_0}{\epsilon\kappa} \tag{2.39}$$

2.2.4.4 The 1-D solution of the Current Continuity Equation and Poisson Equation

Consider the same 1-D geometry of a charged surface. Taking liquid permittivity and conductivity as constant and substituting the Poisson equation into Eq. (2.25), one obtains

$$-D\nabla^2\rho_e + \frac{\sigma}{\epsilon}\rho_e + \nabla\cdot(\rho_e\vec{v}) = 0 \tag{2.40}$$

Taken the velocity as zero, it becomes

$$\nabla^2\rho_e = \frac{\sigma}{D\epsilon}\rho_e \tag{2.41}$$

Noting $\kappa^2 = \frac{\sigma}{D\epsilon}$, one obtains the solution of Eq. (2.41) with the boundary conditions $\rho_e = \rho_{e0}$ at y=0 and ρ_e=0 as $y \to \infty$

$$\rho_e = \rho_{e0}e^{-\kappa y} \tag{2.42}$$

The neutrality of the system gives

$$\int_0^\infty \rho_e e^{-\kappa y}dy + \sigma_0 = 0 \tag{2.43}$$

From Eq. (2.43), one obtains

$$\rho_{e0} = -\kappa\sigma_0 \tag{2.44}$$

Substituting Eq. (2.42) into Poisson equation and solving for ϕ, one obtains

$$\phi = \frac{\sigma_0}{\epsilon\kappa}e^{-\kappa y} \tag{2.45}$$

Substituting Eq (2.39) into Eq. (2.45) gives

$$\phi = \zeta e^{-\kappa y} \tag{2.46}$$

Here the solution of LPB equation is recovered. It suggests that the uniform conductivity approximation and the Debye-Hückel approximation are equivalent. The advantage of Eq. (2.40) is that the net charge distribution is decoupled from potential.

2.3 Numerical method

By solving the set of equations (2.14), (2.17), (2.18) and (2.19) numerically with the appropriate boundary conditions, one obtains the distribution of $\vec{v}$, ϕ and c_i. However, direct numerical simulation would require considerable computational effort to ensure adequate accuracy over the double-layer scale (generally on the order of nanometer) and the largest scale characterized by the channel size (on the order of centimeter). A popular approach is to use a local analytical or numerical solution of Poisson-Boltzmann equation for the double layer region coupled with a numerical solution for the bulk (outside the double layer region). The approach does not consider the effect of the velocity field on the double layer. A direct numerical solution without any simplification has been reported [46, 47], where the geometry is confined to small length to height ratio. For microchannels, the typical intersection scale is on the order of micrometer and the streaming direction scale is on the order of millimeter or centimeter. The liquid conductivity in the bulk can be taken as uniform. The deviation of conductivity can be neglected in the case of low surface charge density. Therefore, liquid conductivity in microchannels can be taken as a constant for a given electrolyte solution. Thus, Eq. (2.25) may be solved instead of Eq. (2.17). Since only one species (the net charge can be treated as a species) is considered, the problem can be simplified and the potential distribution along a microchannel with centimeter in length can be simulated.

2.3.1 Boundary conditions

For an electrokinetic transport system, different types of boundary conditions exist: inlet, outlet, insulator wall, charged surface, or symmetry axis. Boundary conditions for the Navier-Stokes equations are no-slip conditions on the wall. For Poisson equation, convection-diffusion-migration equation or current continuity equation, the prescribed electric potential and species concentrations are imposed for an inlet and outlet. On a charged surface, two kinds of boundary conditions for the electric potential field can be applied: known potential (zeta potential) or known surface charge density. In this work, a known surface charge density is required to solve the governing equations. The normal electric potential is related to the charge density as

$$\frac{\partial \phi}{\partial n} = -\frac{\sigma_0}{\epsilon} \tag{2.47}$$

In order to assure the electrical neutrality of the whole channel, Eq. (2.48) is employed as a control condition for the convection-diffusion-migration equation or the current continuity equation.

$$\sigma_0 + F \sum_i Z_i c_i = 0 \tag{2.48}$$

where σ_0 is surface charge density. The fluxes of all species are zero across a symmetry axis or an insulator wall. For a fully developed parallel-plate microchannel flow (shown in Fig. 2.1), the boundary conditions are:

$$\begin{aligned}
\rho_e &= 0,\ \phi = 0,\ \text{and } p = p_0 \ \ at \ \ x = 0; \\
\rho_e &= 0,\ \phi = \phi_0,\ \text{and } p = 0 \ \ at \ \ x = l; \\
\frac{\partial \phi}{\partial y} &= 0,\ \frac{\partial \rho_e}{\partial y} = 0,\ \frac{\partial u}{\partial y} = 0,\ \frac{\partial v}{\partial y} = 0,\ \text{and } \frac{\partial p}{\partial y} = 0 \ \ at \ \ y = 0; \\
\frac{\partial \phi}{\partial y} &= -\frac{\sigma_0}{\varepsilon},\ u = v = 0,\ \frac{\partial \rho_e}{\partial y} = 0 \text{ and } \frac{\partial p}{\partial y} = 0 \ \ at \ \ y = a; \\
\int \sigma_0 dx &= -\int\int \rho_e dx dy
\end{aligned}$$

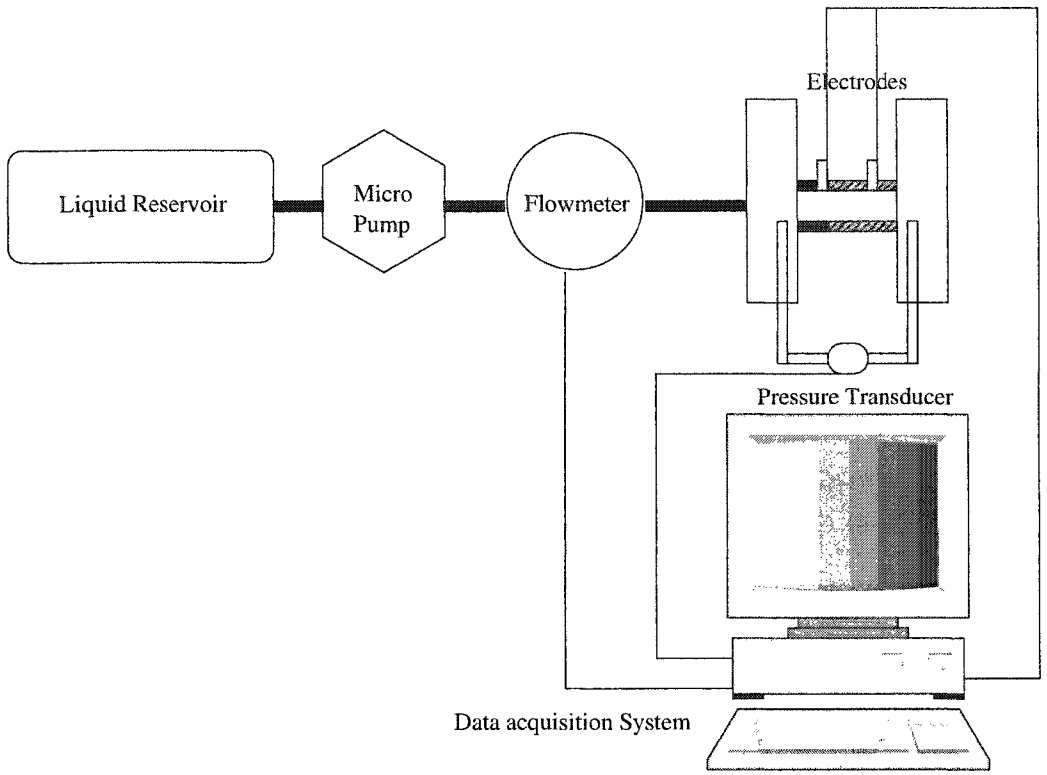

Figure 2.3: Schematic of the experimental system used to measure the electrokinetic properties of pressure-driven flow in parallel-plate microchannels.

u and v are velocities in the x and y direction, respectively. The potential difference ϕ_0 across the length is the value of streaming potential which was determined experimentally. As the solution of our experiment is deionized-ultra-filtered (DIUF) water, a surface charge density of 1.107×10^{-3} C/m^2 was determined (by means of an experimental zeta potential of -86 mV) and was used as the boundary condition.

2.4 Experimental setup

The experimental system used to study electric potential distribution of a liquid flowing through a parallel-plate microchannel is shown in Figure 2.3. This system consists of a flow loop, a test section including a slit microchannel, electrodes, instruments for measuring flow and electrokinetic parameters, and a computer acquisition system. The parallel-plate microchannels were assembled using two identical microscope

slides (Fisher Scientific; catalog No. 12-550A) separated by two thin plastic shims (Small Parts Inc., FL) as spacer for the channel walls. The surface roughness of these slides is on the order of 10 nm. The shims were placed along the lateral edges of the cleaned surfaces and fixed by applying a small amount of epoxy (Devcon, USA), leaving a flow passage of 10 mm wide. Once the channel was formed, it was allowed to dry at room temperature for 12 hours. Subsequently, the width and the length of the microchannel were measured using a precision gauge (Model CD-6"B, Mitutoyo Co., Japan) with an accuracy of ± 1 μm. Finally, the microchannel was mounted by two supporting blocks at the inlet and outlet, respectively, to the setup. The channel height was determined by an indirect method which involves measuring a high concentration electrolyte flow through the microchannel at streaming current mode. At streaming current mode, the two electrodes which were used to measure streaming potential were short-circuited. Therefore, the electrokinetic effects can be eliminated and liquid flow in this case is a Poiseuille flow. The channel height can be calculated by Poiseuille flow equation.

Before the assembly, four cone holes were drilled evenly on the upper plate where platinum electrodes are installed. The diameters of the holes on the glass surface are smaller than those of the electrode to assure that the electrodes do not pass through the upper glass plate and the flow will not be disturbed by the electrodes. Four electrodes were installed evenly onto the upper glass surface. Two other electrodes were inserted near the inlet and outlet into the bulk for streaming potential measurements. In the experiment, a pump (LC-5000, ISCO Inc., USA) was set to maintain a constant flow rate. The readings of the pressure drop along the microchannel were monitored and recorded. A high-impedance electrometer (Keithley Instruments Inc.,Model 6517A) was used here to measure the electric potentials. The flow was considered to have reached a steady state before measurements of the flow rate, pressure drop, bulk liquid conductivity and electric potentials along the channel. The

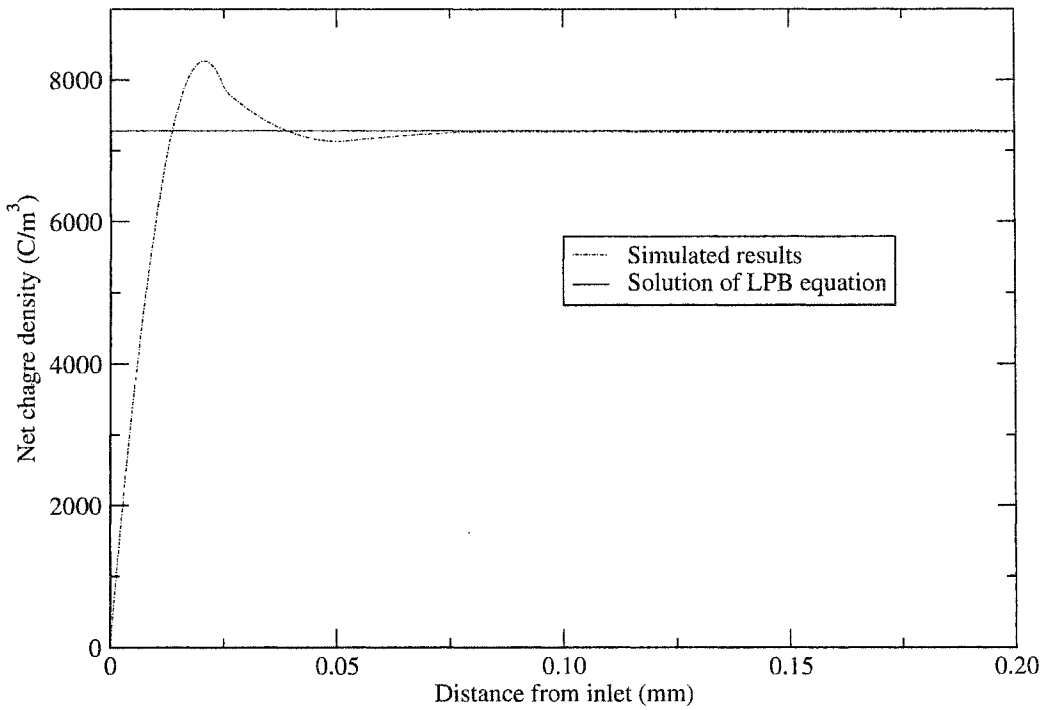

Figure 2.4: The net charge density distribution 50 nm away from the wall along the streamwise direction with Re = 6.6 .

data reported in this thesis are for steady state flow. For a given channel and a given testing liquid, the measurements for all the parameters were repeated at least twice for the same flow rate. After the measurements of one flow rate were completed, the pump was set to a different flow rate and the measurements described above were repeated for the same microchannel.

2.5 Results and discussion

In our study, DIUF water was considered as a binary electrolyte with valences ± 1. The concentration was calculated from its conductivity by means of Eq. (2.23). The following parameters were taken: D=1.0 $\times$ 10^{-9} m^2s^{-1}, ε = 80 $\times$ 8.854 $\times$ 10^{-12} $CV^{-1}m^{-1}$, σ = 1.0 $\times$ 10^{-4} Sm^{-1}. The Debye length (κ^{-1}) calculated from the bulk conductivity of water is 84 nm. Numerical solutions were validated against the analytical solution of the linearized Poisson-Boltzmann (LPB) equation for an equlibrium

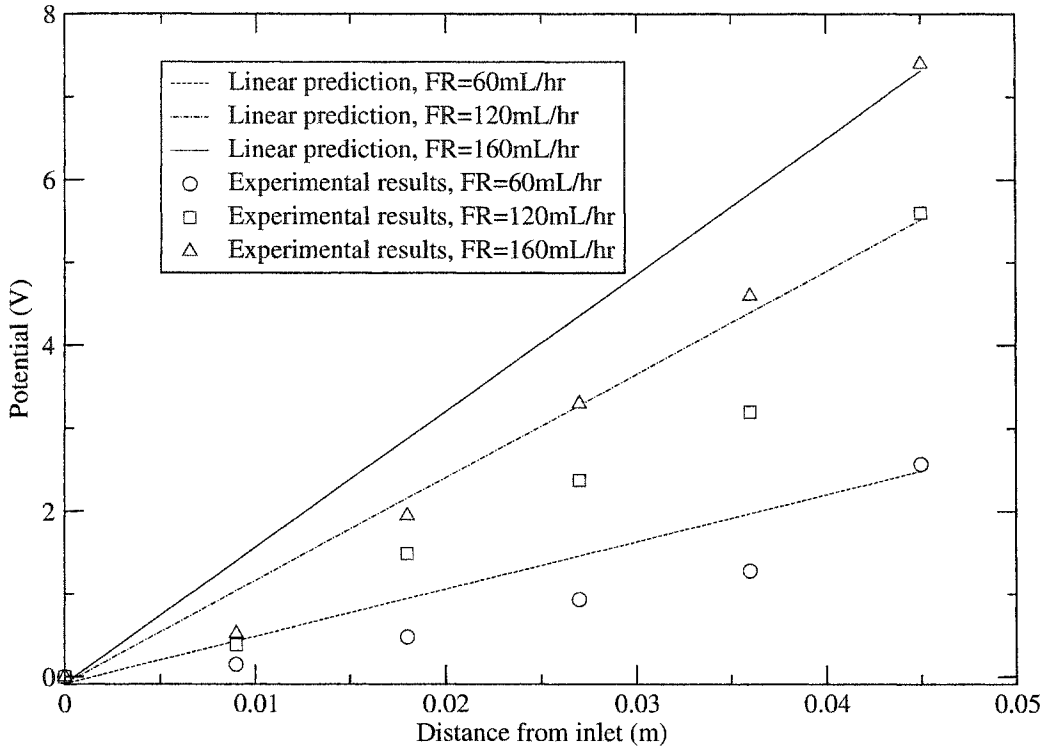

Figure 2.5: Measured potential distribution at different flow rates for DIUF water. The lines correspond to potential distribution predicted by Eq. (2.13). FR denotes the flow rate.

electrical double layer that is adjacent to an infinitely-extended charged surface. The numerical results agreed well with the analytical solutions of LPB equation without external fields. With the introduction of a flow field, the net charge density distribution will be influenced by the flow field. Figure 2.4 shows the net charge density distribution 50 nm away from the wall along the streamwise direction with a Reynolds number (Re) of 6.6. The net charge density distribution follows the solution of LPB equation on the region far from the inlet. The growth of net charge on the entry region is clearly demonstrated in Figure 2.4.

Figure 2.5 displays the measured potential distribution across the inlet and outlet near the surface for three flow rates: 60, 120 and 160 mL/hr. Our procedures to determine the streaming potential are consistent with those in the literature by other

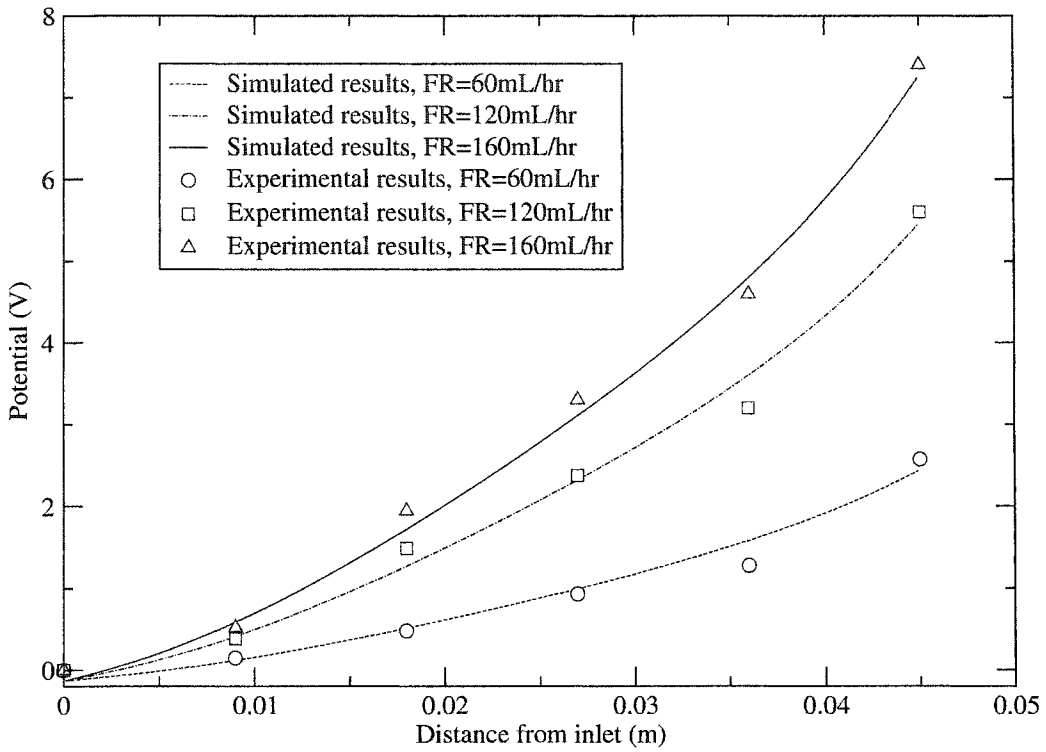

Figure 2.6: Comparison of the experimental and simulated potential distribution downstream along a parallel-plate channel of 40 μm (height) $\times$ 10 mm (width) $\times$ 4.5 cm (length) for DIUF water. The simulated results were obtained by the current continuity equation with a charge density of 1.107 $\times$ 10^{-3} C/m^2 as the boundary condition.

authors [42, 69, 70]. The straight lines are predicted potential distribution near the interface along the streamwise direction according to Eq. (2.13). If assumed that there is no net charge in the bulk, the lines connecting directly the inlet and outlet potentials in Figure 2.5 represent the potential distribution in the bulk along the channel. If the distribution is linear, one would also expect those on the surface to follow a straight-line relationship. Figure 2.6 shows the experimental and simulated potential distribution near the solid-liquid interface along the channel for different flow rates. It can be seen that the measured absolute potential values near the interface do not follow the linear relationship shown in Figure 2.5; rather, they are non-linear and smaller than those predicted by Eq. (2.13), suggesting that the potential difference

between the interface and bulk is larger than that predicted by the Poisson-Boltzmann equation. It should be noted that the three curves in Figure 2.6 were not curve-fitted, but our simulated results using an experimentally determined charge density of 1.107 $\times$ 10^{-3} C/m^{-2} as the boundary condition. The phenomenon shown in Figures 2.5 and 2.6 can be explained as follows.

The discussion is started from the physical mechanism of streaming potential. Based on Helmholtz's theory, streaming potential is caused by direct movement of electrical charges. However, the continue transfer of electrical charges in liquid does not necessarily cause a potential gradient. This is easily illustrated by the fact that there exists no potential gradient along the channel in streaming current mode in which the terminal electrodes are short-circuited. In this case, a streaming current will result without any potential difference in the streamwise direction. Hunter [18] stated that accumulation of charges downstream sets up an electric field. If this is true, there must be a charge density gradient in the streaming direction. Hence, the mechanism of streaming potential can be explained as follows: at static state (no flow), ions distribute themselves in EDL as described by the Boltzmann distribution. When a flow field is introduced, hydrodynamic force will drag the diffusion layer downstream. This diffusion layer in EDL near the inlet will be replaced by neutral liquid temporarily. Since charges on the solid surface are immobile, movement of ions in EDL will cause accumulation of charges downstream and the deficit of counterions upstream temporarily. At this instant, charges on the solid surface upstream and the accumulated charges downstream will draw back counterions and push away coions from the EDL and liquid bulk, in attempt to recover the initial EDL structure. This effect will cause a migration flux (conduction current) in both streamwise x and height y directions. With respect to the conduction current in streamwise direction x, a potential difference will result which is the so-called streaming potential. With respect to the conduction current in the height direction y, a potential difference will

buildup across the channel and the potential at the shear plane is the so-called zeta potential. When the net current becomes zero, equilibrium is established. The net current then consists of streaming, conduction and diffusion currents; hence, a steady state is characterized by the equilibrium of these three currents. Thus, the electric field along and across the channel is established by the solid surface charges and the charge redistribution in EDL caused by the streaming current in the channel. In streaming current measurements, on the other hand, since the streaming current at the outlet is conducted back through an outside short-circuit to the entrance, the flow of net charge (streaming current) will not cause similar charge redistribution as in the streaming potential measurements. In streaming current measurements, the electric field in streamwise direction produced by surface charges is balanced by the electric field resulting from the net charge in EDL. Thus, in streaming current mode, there is no potential difference in streamwise direction and, hence, the EDL structure can be assumed to be the same as the static state.

As described earlier, in the case of streaming potential measurements, a conduction current will be produced in both height y and streamwise x directions by an electric field resulting from solid surface charges and charge redistribution in EDL. If the conduction current in height direction y is different from that in the static state, the potential difference between the EDL and the bulk will be different from that predicted by the Poisson-Boltzmann equation. Figures 2.5 and 2.6 indicate that the average conduction current ($\frac{|\phi_{sf}-\phi_B|\sigma}{a}$) in the height direction y in the presence of flow field is much larger than that in the static state. From our previous discussion, it is expected that the streaming current is equilibrated by both the diffusion and conduction currents. If the diffusion current is equilibrated exactly by the conduction current in the height direction y, the streaming current will be equilibrated by the conduction current in streamwise direction. In this case, the zeta potential determined from both streaming potential and streaming current methods would be identical. Otherwise,

the streaming current will be partially equilibrated by the diffusion and/or conduction currents in the height direction y; the conduction current in the streamwise direction is only a fraction of the streaming current. In the literature, when Eq. (2.10) is used to derive the relationship between zeta and streaming potentials, the conduction current I_c is considered as the conduction current in the streamwise direction. If the conduction current in streamwise direction is only a fraction of the streaming current as shown above, the zeta potential determined from streaming potential and streaming current methods would be different. This discrepancy has frequently been ascribed to the variation of surface conductance. From the results presented here, it is found that the variation of EDL structure due to flow field may result in the same effect. According to the Poisson equation, the presence of net charge will cause nonlinearity of potential distribution, as confirmed from the experimental results in Figure 2.6. In this Figure, it is found that the predicted potential distribution near the interface by numerical simulation agrees reasonably well with those from experiments. When the channel size becomes smaller, it is expected that the flow field effect on EDL structure will be stronger. This flow field effect may explain the unusual behavior of streaming potential in geometries where the characteristic dimensions are comparable to the Debye length.

2.6 Conclusions

The effects of flow field on the electric double layer distribution for a dilute electrolyte (DIUF water) in a streaming potential mode have been studied experimentally and numerically. The experimental results show that the average conduction current across the channel with introduction of a flow field is larger than that from the static EDL model. The numerical simulation shows that the potential distribution in streamwise direction in EDL can be non-linear. These results in this chapter indicate that the conduction current in streamwise direction is only a fraction of the streaming

current. Therefore, the zeta potential values determined from streaming potential measurements are generally smaller than those from streaming current measurements for dilute electrolytes. This discrepancy has frequently been ascribed to the variation of surface conductance and the effect of surface conductance on the streaming potential measurements would have been over-estimated when κa is small.

Chapter 3

Pressure-driven Electrokinetic Flow in Porous Media

3.1 Introduction

When a porous medium, composed of solid bed particles, is immersed in a dilute electrolyte, the solid particles will be charged and EDL will form in the region adjacent to the particle surface. This region is called the Debye sheath layer. When a macroscopic pressure gradient is applied to the porous medium, the fluid percolates through it with a Darcy seepage velocity. The continuous transport of net charge in the Debye sheath layer will create a macroscopic electric current which is called streaming current. An electric field is generated to cause a conduction current to equilibrate the streaming current. The electric field will cause an additional body force acting on the electrolyte in the Debye layer, resulting a reduced volume flow rate. This is pressure-driven electrokinetic flow. On the other hand, when a porous material, saturated with the electrolyte, is embodied in an external electric field, the body force acting on the electrolyte in the Debye layer will cause the electrolyte in the porous medium to flow. This is the so-called electroosmotic flow.

Electrokinetic effects in porous media have been investigated by various models. The two main descriptions are capillary tube models and unconsolidated packings of particles. The transport properties of circular capillaries were studied by many authors [23, 24, 71, 72]. The Debye length effect and zeta potential effect have been

discussed in these papers. Kuin and Stein [73] investigated various types of periodically constricted channels which represented more closely the flow path in a porous medium. In the limit of thin Debye length, the transport properties of packed beds were studied by O'Brien *et al.* [74, 75, 76]. As mentioned in Chapter 2, the most popular approach on electrokinetic effects is decoupled potential approach. In this approach, the EDL structure is determined by local potential gradient which may be obtained by solving the Possion-Boltzmann equation. The effect of flow field and external or flow-induced electric field on EDL structure was ignored. In Chapter 2, the effect of flow field on the EDL in parallel-plate microchannels has been demonstrated. In this Chapter, the effect of flow-induced electrical field on the EDL will be demonstrated.

In this Chapter, an electrical circuit model which follows the classical approach is proposed for more general time-dependent flow in a single microchannel; the results are employed to construct the governing equations for a multichannel model. The electric potential and current were measured for pressure-driven flow in different pore size porous media with an external load. By comparing the predicted results and those from experiment, good agreement was found in the limit of thin double layers; larger deviation was obtained when the Debye length was comparable with the pore size.

3.2 Electrokinetic flow and electric circuit analysis of a single microchannel

3.2.1 Controlling equations and boundary conditions

Consider a model for pressure-driven and time-dependent electrokinetic flow through a single circular microchannel. For an individual microchannel without an external circuit, the boundary value problem for oscillating liquid flow in an infinitely extended circular microchannel is considered. A cylindrical coordinate system (r, θ, z) is used

where the z-axis is taken to coincide with the microchannel central axis. All field quantities are taken to depend on the radial coordinate r and time t. The boundary value problem with the relevant field equations and boundary conditions are described below.

3.2.2 Electrical field

The total potential ϕ at location (r, z) at a given time t is taken to be

$$\phi \equiv \phi(r, z, t) = \psi(r) + [\phi_0 - zE_z'(t)] \ , \tag{3.1}$$

where $\psi(r)$ is the potential due to the double layer at equilibrium state (i.e., no liquid motion with no applied external field); ϕ_0 is the potential at $z = 0$ (i.e., $\phi_0 \equiv \phi(r, 0, t)$); and $E_z'(t)$ is the spatially uniform, time-dependent electric field strength. The total potential ϕ in Eq. (3.1) is axisymmetric and, when $E_z'(t)$ is time-independent, Eq. (3.1) is identical to Eq. (6.1) of [77]. The time-dependent flow to be studied here is assumed to be sufficiently slow such that the radial charge distribution is relaxed at its steady state. Further, it is assumed that any induced magnetic fields are sufficiently small and negligible such that the total electric field may still be defined as $-\vec{\nabla}\phi$ [78]; this definition can then be used to obtain the Poisson equation

$$\nabla^2\phi = -\frac{\rho_e}{\epsilon} \ , \tag{3.2}$$

where ρ_e is the free charge density and ϵ is the permittivity of the medium. Combining Eqs. (3.1) and (3.2) yields the following Poisson equation in cylindrical coordinate

$$\frac{1}{r}\frac{d}{dr}\left(r\frac{d\psi(r)}{dr}\right) = -\frac{\rho_e}{\epsilon} \ . \tag{3.3}$$

The conditions imposed on $\psi(r)$ are

$$\psi(a) = \psi_s \qquad \text{and} \qquad \psi(0) \text{ is finite} \ , \tag{3.4}$$

where ψ_s is the surface potential at the capillary wall, $r = a$; a is the radius of the microchannels. For brevity, a symmetric, binary electrolyte with univalent charges is considered. The cations and anions are identified as species 1 and 2, respectively. Based on the assumption of thermodynamic equilibrium, the Boltzmann equation provides a local charge density ρ_{ei} of the ith species. Thus

$$\rho_{ei} = Z_i e n_\infty \exp\left[-\frac{Z_i e \psi}{kT}\right] , \qquad (i = 1, 2) , \tag{3.5}$$

where Z_i is the valence of the ith species; e is the elementary charge; n_∞ is the ionic concentration in an equilibrium electrochemical solution at the neutral state where $\psi = 0$; k is the Boltzmann constant; and T is the absolute temperature. Invoking the Debye-Hückel approximation for low surface potentials ($Z_i e\psi/kT << 1$), one has $\sinh(Z_0 e\psi/kT) \approx Z_0 e\psi/kT$ and the total charge density follows from Eqs. (3.3) and (3.5) as

$$\rho_e = \sum_{i=1}^{2} \rho_i = \frac{-2n_\infty e^2 Z_0^2}{kT}\psi , \tag{3.6}$$

where $Z_1 = -Z_2 = Z_0$ is used. Finally, the definition of the reciprocal of the double layer thickness for a $(Z_0 : Z_0)$ electrolyte is given as

$$\kappa = \sqrt{\frac{2n_\infty e^2 Z_0^2}{\epsilon kT}} . \tag{3.7}$$

Combining Eqs. (3.3) and (3.6) results in

$$\frac{1}{r}\frac{d}{dr}\left(r\frac{d\psi(r)}{dr}\right) = \kappa^2\psi ,$$
$$\psi(a) = \psi_s \quad \text{and} \quad \frac{\partial\psi(0)}{\partial r} = 0 \tag{3.8}$$

3.2.3 Hydrodynamic field

The axial electric field will induce a body force $\rho_e E_z'$ and the modified Navier-Stokes equation in the axial direction (or z-direction) becomes

$$-\frac{1}{\mu}\frac{\partial p}{\partial z}+\frac{1}{r}\frac{\partial}{\partial r}\left(r\frac{\partial v}{\partial r}\right)+\frac{1}{\mu}\rho_e E_z'=\frac{1}{\nu}\frac{\partial v}{\partial t}\ , \tag{3.9}$$

where the pressure gradient $[\frac{\partial p}{\partial z}\equiv\frac{\partial p}{\partial z}(t)]$ is taken to be position-independent; v is the velocity in axial direction (z-direction); μ is the viscosity; ρ_e is the total charge density and ν is the kinematic viscosity of the liquid. The boundary conditions for the velocity field are

$$v(a,t)=0 \quad \text{and} \quad \frac{\partial v(0,t)}{\partial r}=0\ , \tag{3.10}$$

The electric current density along the microchannel may be integrated over the channel cross-section to give the electric current

$$I=2\pi\int_0^a \rho_e v r dr+\frac{E_z' L}{\overline{R}}\ , \tag{3.11}$$

where

$$\overline{R}=\frac{R_0 R_s}{R_0+R_s}\ ,$$

$\overline{R}$, R_0, R_s and L are the total resistance, bulk electrolyte resistance, surface resistance and the microchannel length, respectively. The first term on the right side of Eq. (3.11) is due to bulk convection and the second term to conduction current. Because of the assumption of an infinitely extended microchannel, the contribution to the current due to concentration gradients vanishes. Using Eq. (3.5) for a $(Z_0 : Z_0)$ electrolyte, one has $\rho_1-\rho_2=2eZ_0 n_\infty \cosh(Z_0 e\psi/kT)$. The Debye-Hückel approximation implies that $\cosh(Z_0 e\psi/kT)\approx 1$ and $\rho_1-\rho_2=2Z_0 e n_\infty$. With this simplification,

the conductivity of bulk electrolyte K_b can be written as

$$K_b = \frac{2Z_0^2 e^2 n_\infty D}{kT} \ , \tag{3.12}$$

where D is the diffusion coefficients of ions. The resistances R_0 and R_s are defined as

$$R_0 = \frac{L}{K_b \pi a^2} \ , \quad R_s = \frac{L}{K_\sigma P_w} \tag{3.13}$$

where K_σ is the surface conductivity and $P_w = 2\pi a$ is the wetted perimeter. The flow rate q can be written as

$$q = 2\pi \int_0^a vr dr \ . \tag{3.14}$$

3.2.4 Analytical solution

An analytical solution is sought here for a sinusoidal periodicity in the electrohydrodynamic fields and this is best addressed by using complex variables. Thus, a general field quantity X may be defined as the real part of the complex function $(X^* e^{j\omega t})$ where X^* is complex $(j = \sqrt{-1})$, ω is the oscillation frequency oscillation, and t is the time. The general field quantity X is written as

$$X = Re[X^* e^{j\omega t}] \ . \tag{3.15}$$

The phase angle ω is defined as

$$\omega = \tan^{-1} \frac{Im(X^*)}{Re(X^*)} \ , \tag{3.16}$$

where $Im(X^*)$ and $Re(X^*)$ are the imaginary and real parts of X^*, respectively. An alternative representation of Eq. (3.15) is given as

$$X = Re[|X^*| e^{j(\omega t + \phi)}] \quad ,$$

where

$$|X| = |X^*| \text{ and } |X^*| = \sqrt{Im^2(X^*) + Re^2(X^*)} \tag{3.17}$$

With the notation of Eq. (3.15), the solution of the boundary value problem for the following specific dependencies will be sought

$$-\frac{\partial p}{\partial z} = Re[p^* e^{j\omega t}] \quad , \quad E'_z = Re[E^*_z e^{j\omega t}] \ . \tag{3.18}$$

Consider the class of solutions where the amplitude of the pressure gradient and the electric field could be frequency-dependent, i.e., $p^* \equiv p^*(\omega)$ and $E^*_z \equiv E^*_z(\omega)$. The solution for ψ will then follow from Eq. (3.8) and that for v from Eq. (3.9). Thus

$$v = Re[v^* e^{j\omega t}] \quad ,$$

where

$$v^* \equiv v^*(r,\omega) = v^*_p(r,\omega)p^*(\omega) + v^*_E(r,\omega)E^*_z(\omega) \tag{3.19}$$

The expression for $v^*_p(r,\omega)$ and $v^*_E(r,\omega)$ will be given at the end of this section. The electric current will follow from Eq. (3.11) and may be written as

$$I = Re[I^* e^{j\omega t}]$$

where

$$I^* \equiv I^*(\omega) = I^*_p(\omega)p^*(\omega) + I^*_E(\omega)E^*_z(\omega) \ . \tag{3.20}$$

The volumetric flow rate q is defined in Eq. (3.14) and can be expressed as

$$q = Re[q^* e^{j\omega t}]$$

where

$$q^* \equiv q^*(\omega) = q_p^*(\omega)p^*(\omega) + q_E^*(\omega)E_z^*(\omega) \ . \tag{3.21}$$

During pressure-driven-flow, the amplitude of the streaming potential $E_z^*(\omega)$ is found by setting $i^* = 0$ in Eq. (3.20). Thus

$$E_z^*(\omega) \ = \ -\frac{I_p^*(\omega)}{I_E^*(\omega)}p^*(\omega) \ \text{ for } \ I^* = 0 \ . \tag{3.22}$$

Equation (3.22) may be substituted into Eqs. (3.19) and (3.21) to determine the normalized liquid velocity and the volumetric flow rate, respectively. Alternatively, the velocity, current and volumetric flow rate during electroosmosis flow follow from Eqs. (3.19)–(3.21) by setting $p^*(\omega) = 0$.

The relevant quantities in Eqs. (3.19)–(3.21) are listed below

$$v_P^*(r,\omega) \ = \frac{1}{j\omega\rho_d}\left[1 - \frac{J_0\left(r\sqrt{\frac{-j\omega}{\nu}}\right)}{J_0\left(a\sqrt{\frac{-j\omega}{\nu}}\right)}\right] \ , \tag{3.23}$$

$$v_E^*(r,\omega) \ = \frac{\epsilon\kappa^2\psi_s}{(\kappa^2\nu - j\omega)\rho_d}\left[\frac{J_0(j\kappa r)}{J_0(j\kappa a)} - \frac{J_0\left(r\sqrt{\frac{-j\omega}{\nu}}\right)}{J_0\left(a\sqrt{\frac{-j\omega}{\nu}}\right)}\right] \ , \tag{3.24}$$

$$\begin{aligned} I_p^*(\omega) = & \frac{2\pi\epsilon\kappa^2\psi_s}{\rho_d}\left\{\frac{a}{\omega\kappa}\frac{J_1(j\kappa a)}{J_0(j\kappa a)}\right. \\ & \left. - \frac{\nu a}{\omega^2 + j\omega\kappa^2\nu}\left[j\kappa\frac{J_1(j\kappa a)}{J_0(j\kappa a)} - \sqrt{\frac{-j\omega}{\nu}}\frac{J_1\left(a\sqrt{\frac{-j\omega}{\nu}}\right)}{J_0\left(a\sqrt{\frac{-j\omega}{\nu}}\right)}\right]\right\} \ , \end{aligned} \tag{3.25}$$

$$I_E^*(\omega) = \frac{-2\pi\epsilon^2\kappa^4\psi_s^2}{(\kappa^2\nu - j\omega)\rho_d}\left\{\frac{a^2}{2}\left[1+\frac{J_1^2(j\kappa a)}{J_0^2(j\kappa a)}\right]\right.$$
$$\left. - \frac{\nu a}{j\omega - \kappa^2\nu}\left[j\kappa\frac{J_1(j\kappa a)}{J_0(j\kappa a)} - \sqrt{\frac{-j\omega}{\nu}}\frac{J_1\left(a\sqrt{\frac{-j\omega}{\nu}}\right)}{J_0\left(a\sqrt{\frac{-j\omega}{\nu}}\right)}\right]\right\} + \frac{L}{\overline{\overline{R}}}, \tag{3.26}$$

$$q_p^*(\omega) = \frac{2\pi}{j\omega\rho_d}\left[\frac{a^2}{2} - \frac{a}{\sqrt{\frac{-j\omega}{\nu}}}\frac{J_1\left(a\sqrt{\frac{-j\omega}{\nu}}\right)}{J_0\left(a\sqrt{\frac{-j\omega}{\nu}}\right)}\right], \tag{3.27}$$

$$q_E^*(\omega) = \frac{2\pi\epsilon\kappa^2\psi_s}{(\kappa^2\nu - j\omega)\rho_d}\left[\frac{a}{j\kappa}\frac{J_1(j\kappa a)}{J_0(j\kappa a)} - \frac{a}{\sqrt{\frac{-j\omega}{\nu}}}\frac{J_1\left(a\sqrt{\frac{-j\omega}{\nu}}\right)}{J_0\left(a\sqrt{\frac{-j\omega}{\nu}}\right)}\right]. \tag{3.28}$$

where J_0, J_1 ρ_d and ν are the zeroth- and first-order Bessel functions of the first kind, liquid density and kinematic viscosity, respectively. By defining the first term of $I_E^*(\omega)$ as $I_{E,1}^*(\omega)$, it can be expressed as

$$I_{E,1}^*(\omega) = \frac{-2\pi\epsilon^2\kappa^4\psi_s^2}{(\kappa^2\nu - j\omega)\rho_d}\left\{\frac{a^2}{2}\left[1+\frac{J_1^2(j\kappa a)}{J_0^2(j\kappa a)}\right]\right.$$
$$\left. - \frac{\nu a}{j\omega - \kappa^2\nu}\left[j\kappa\frac{J_1(j\kappa a)}{J_0(j\kappa a)} - \sqrt{\frac{-j\omega}{\nu}}\frac{J_1\left(a\sqrt{\frac{-j\omega}{\nu}}\right)}{J_0\left(a\sqrt{\frac{-j\omega}{\nu}}\right)}\right]\right\} \tag{3.29}$$

The streaming current I_s is defined as the first term of Eq.(3.11) or $I_s = Re[(I_p^* p^* + I_{E,1}^* E_z^*)e^{j\omega t}] = Re[I_s^* e^{j\omega t}]$.

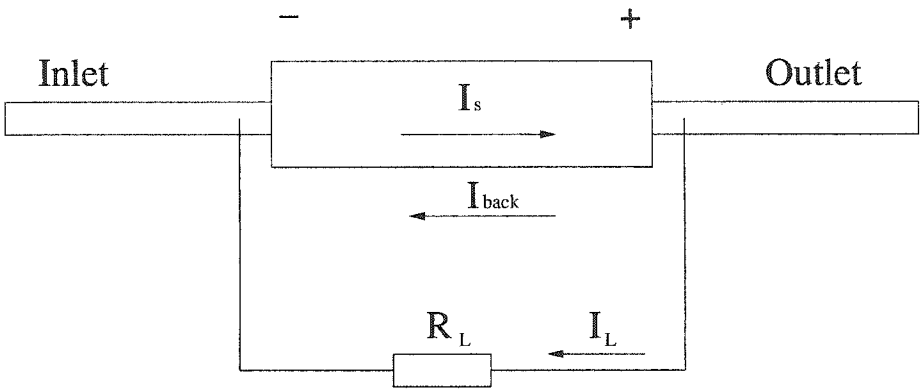

Figure 3.1: Schematic diagram of a multi-channel array circuit

When $\omega \to 0$, Eqs.(3.23)-(3.28) reduce to those of steady state.

$$
\begin{aligned}
v_p^*(r,0) &= \frac{1}{4\nu\rho_d}(a^2 - r^2) \ , \\
v_E^*(r,0) &= -\frac{\epsilon\psi_s}{\nu\rho_d}\left(1 - \frac{J_0(j\kappa r)}{J_0(j\kappa a)}\right) \ , \\
I_p^*(0) &= -\frac{\epsilon\psi_s\pi a^2}{\nu\rho_d}\left[1 - \frac{2}{j\kappa a}\frac{J_1(j\kappa a)}{J_0(j\kappa a)}\right] \ , \\
I_E^*(0) &= -\frac{\epsilon^2\psi_s^2\pi a^2\kappa^2}{\nu\rho_d}\left[1 - \frac{2}{j\kappa a}\frac{J_1(j\kappa a)}{J_0(j\kappa a)} + \frac{J_1^2(j\kappa a)}{J_0^2(j\kappa a)}\right] + \frac{L}{\overline{\overline{R}}} \ , \\
q_p^*(0) &= \pi a^2 \frac{a^2}{8\nu\rho_d} \ , \\
q_E^*(0) &= -\frac{\epsilon\psi_s\pi a^2}{\nu\rho_d}\left[1 + 2\frac{jJ_1(j\kappa a)}{\kappa a J_0(j\kappa a)}\right] \ , \\
I_{E,1}^*(0) &= -\frac{\epsilon^2\psi_s^2\pi a^2\kappa^2}{\nu\rho_d}\left[1 - \frac{2}{j\kappa a}\frac{J_1(j\kappa a)}{J_0(j\kappa a)} + \frac{J_1^2(j\kappa a)}{J_0^2(j\kappa a)}\right] \ .
\end{aligned}
\tag{3.30}
$$

3.3 Circuit analysis of multi-microchannel array

Since the streaming current of a single microchannel is small and of the order of nano amphere, n microchannels are combined to obtain a larger current for an external load R_L. Consider a pressure-driven flow in a porous medium with an external circuit in Figure 3.1. The pressure-driven flow in microchannels will cause a streaming current I_s. Since the liquid itself is a conductor, a fraction of the streaming current I_{back} will

conduct back by the liquid and the other part I_L will pass through external resistance R_L. At equilibrium,

$$I_s = I_{back} + I_L \tag{3.31}$$

From circuit analysis, one knows that the potential difference U_L across the channel and the potential drop across the external resistance must be same.

$$U_L = I_{back}\overline{R} = I_L R_L \tag{3.32}$$

where $\overline{R}$ is the total resistance of the microchannels which includes bulk resistance and surface resistance. When $R_L \to 0$, all streaming current will conduct through an external circuit and this corresponds to a streaming current mode. When $R_L \to \infty$, all streaming current will conduct back through the liquid and the potential difference across the channel is the streaming potential U_{str} (streaming potential mode).

By changing the load resistance when flow rate is fixed, the U_L and I_L will change. Combining Eq. (3.31) with Eq. (3.32) gives

$$U_L = \overline{R}(I_s - I_L) \tag{3.33}$$

Considering

$$I_s = I_p^*(0)\frac{\Delta P}{L} + I_{E,1}^*(0)\frac{U_L}{L} \tag{3.34}$$

one can solve for U_L as

$$U_L = \frac{(\alpha q - I_L)\overline{R}}{1 + \beta\overline{R}} \tag{3.35}$$

where $\alpha = \frac{8\nu\rho_d I_p^*(0)}{N\pi a^4}$ and $\beta = \frac{I_{E,1}^*(0)}{L} - \frac{8\nu\rho_d}{N\pi a^4 L} I_p^*(0) q_E^*(0)$. For a given geometry and flow rate, α, β and $\overline{R}$ are constant. Equation (3.33) predicts a linear relationship between U_L and I_L when R_L changes.

3.4 Experimental section

The experimental system used to study pressure-driven electrokinetic flow in porous media is shown in Figure 3.2. This system consists of a flow loop, a test section including microchannels, silver mesh electrodes, a load circuit, instruments for measuring flow and electrokinetic parameters, and a computer acquisition system. A porous ceramic rod or disk (Small Parts Inc. and Soilmoisture Equipment Corp.) is employed as source of porous media for electrokinetic generation. Two electrodes consisting of a silver meshed network were placed at the two ends of the ceramic rod or disk and in connection with the load resistor. The resistor can change from 100 kΩ to 10 MΩ. All other connections are plastic or Teflon which can be considered as good insulators. Deionized ultrafiltered (DIUF) water (Fisher Scientific) with a conductivity of 1.0×10^{-4} S/m was employed as the working liquid. In the experiment, a pump (LC-5000, ISCO Inc., USA) was set to maintain a constant flow rate. The readings of the pressure drop across the filter were monitored and recorded. A high-impedance electrometer (Keithley Instruments Inc., Model 6517A) was employed here to measure the electric potentials across the resistor and the same electrometer was employed to measured the current after the potential was measured. The flow was considered to have reached a steady state before measurements of the flow rate, pressure drop, electric potentials and electric current. The data reported in this thesis are for steady state flow.

The experiment was conducted once daily, at approximately the same time every day, for a period of at least six days. First, with no external resistance connected in the circuit, water is pumped through the filter for a period of one hour, or until the streaming potential becomes stable. Throughout this initial run, the streaming potential is recorded as it varies over time. Without stopping the water pump, a variable resistor (here with five resistance settings) is then attached to the circuit in

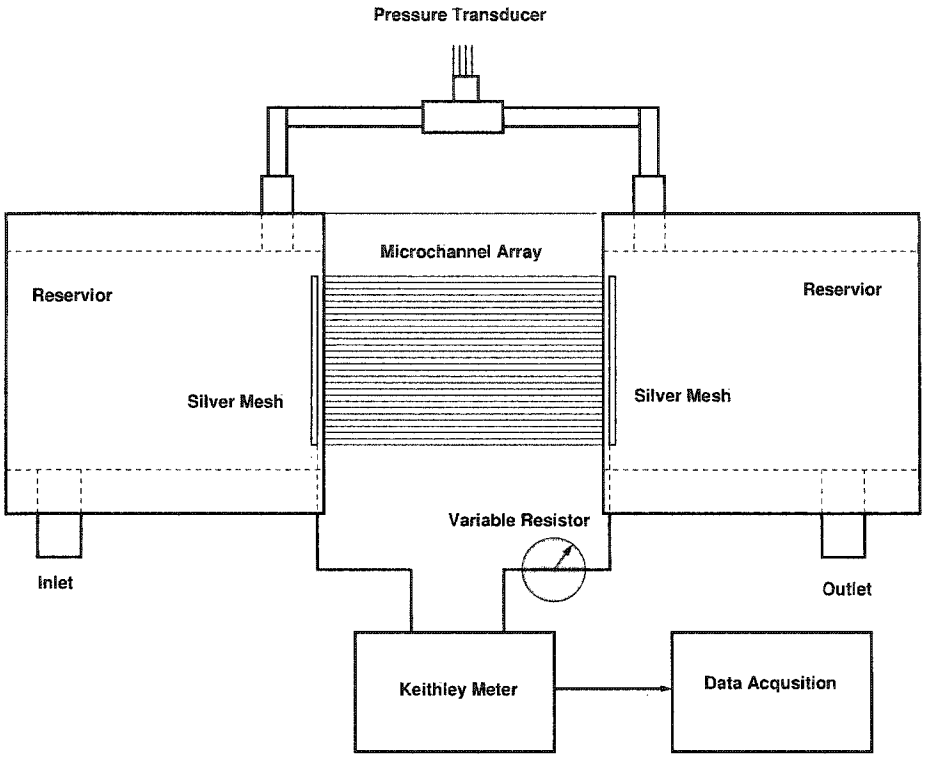

Figure 3.2: Schematic of the experimental system

parallel to the electrometer. Initially, the variable resistor is set to its lowest setting. Potential drop on the resistor is then recorded for the length of time required to obtain enough data points in the LabView program. Once sufficient data points are gathered, the resistance is incremented and the data gathering process is repeated. After the data for the final resistance setting is gathered, the variable resistor is removed from the circuit. Without stopping the water pump, the variable resistor is attached to the circuit in series as shown in Figure 3.2 . The electrometer is switched to a current mode. The variable resistor is reset to its highest setting. The current in the circuit is then recorded for the length of time required to obtain sufficient data points in the LabView program. Once sufficient data points are gathered, the resistance is switched to a lower one and the data gathering process is repeated. After the data for the final resistance is gathered, the experiment is finished for one day. In the experiment, the

Table 3.1: The ceramic filters used in the experiment

Sample	Maximum pore size (μm)	Dimensions D (mm)$\times$ L (mm)	Company
1	6	12.5$\times$ 50	Smallparts
2	2.5	25$\times$ 50	Smallparts
3	2.5	25 $\times$ 50	Soilmoisture
4	0.16	15.88 $\times$ 7.14	Soilmoisture

measured potential drop and current were checked by Ohm's law. The ceramic filters used in the experiment together with their physical dimensions are listed in Table 3.1.

Table 3.2: The average size, number of pores and measured zeta potential of the ceramic filters used in the experiment

Sample	Average pore radius $a(\mu$m)	Number of pores	κa	Zeta potential (mV)
1	1.748	6.39×10^6	20.8	-19.9
2	0.727	1.33×10^8	8.7	-16.2
3	0.581	2.09×10^8	6.9	-27.5
4	0.061	5.48 $\times10^9$	0.7	-1.9

The number of pores in the ceramic filter N can be calculated from

$$N = \eta \frac{A}{\pi a^2} \tag{3.36}$$

where η is the porosity of the filter and A is the effective area of the filter. In streaming current mode, the flow rate can be expressed as

$$q = N \frac{\pi a^4 \Delta P}{8 \nu \rho_d L} \tag{3.37}$$

From the measured flow rate and pressure drop in streaming current mode, the number of pores and the average pore size of the filter can be calculated by combining Eqs. (3.36) and (3.37). The measured average pore size and number of pores of the filters are listed in Table 3.2. The following parameters were employed in our calcu-

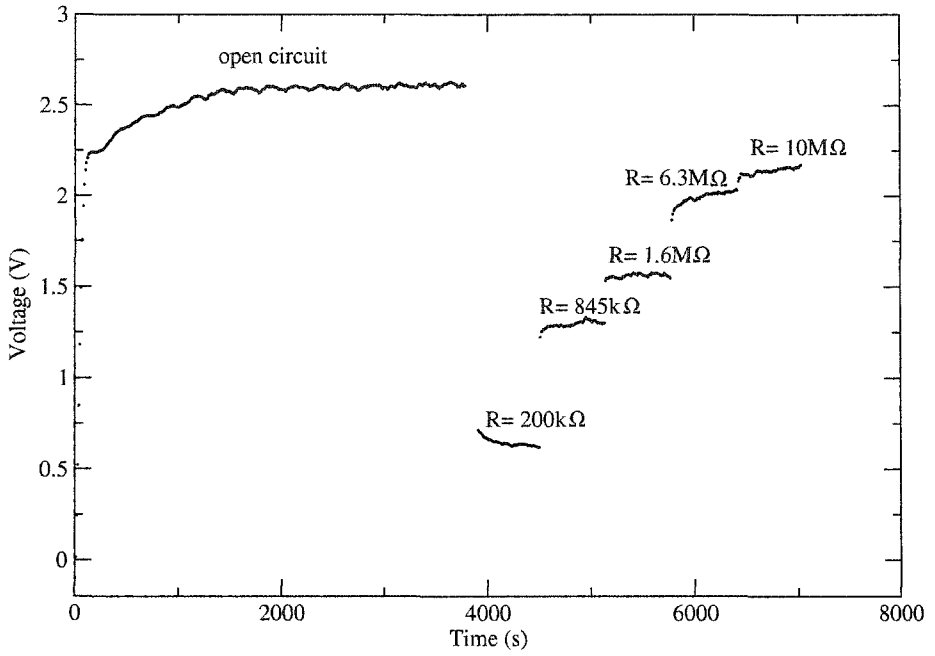

Figure 3.3: Typical potential versus time curve with different loadings

lation: $\epsilon = 80 \times 8.854 \times 10^{-12}$ $CV^{-1}m^{-1}$, $\nu = 0.9 \times 10^{-6}$ m^2s^{-1}, $\rho_d = 10^3$ kgm^{-3}, and $\kappa = 1.19 \times 10^7$ m^{-1}. The typical potential versus time curve and current versus time curve with different loadings are shown in Figures 3.3 and 3.4, respectively.

3.5 Results and discussion

The zeta potentials of the filters can be measured by streaming potential or streaming current method. Since the pore size is comparable with the Debye length, it is not sufficient to measure one streaming potential calculation of the zeta potential: a second measurement to find surface conduction is also needed in streaming potential method. Since surface conduction is expected to depend on κa and concentration of liquid [79], it is not easy to obtain accurate surface conduction for a specific filter. Therefore, the streaming current method is employed to measure the zeta potential. From the expression of $I_p^*(0)$ in streaming current mode, one may obtain the zeta

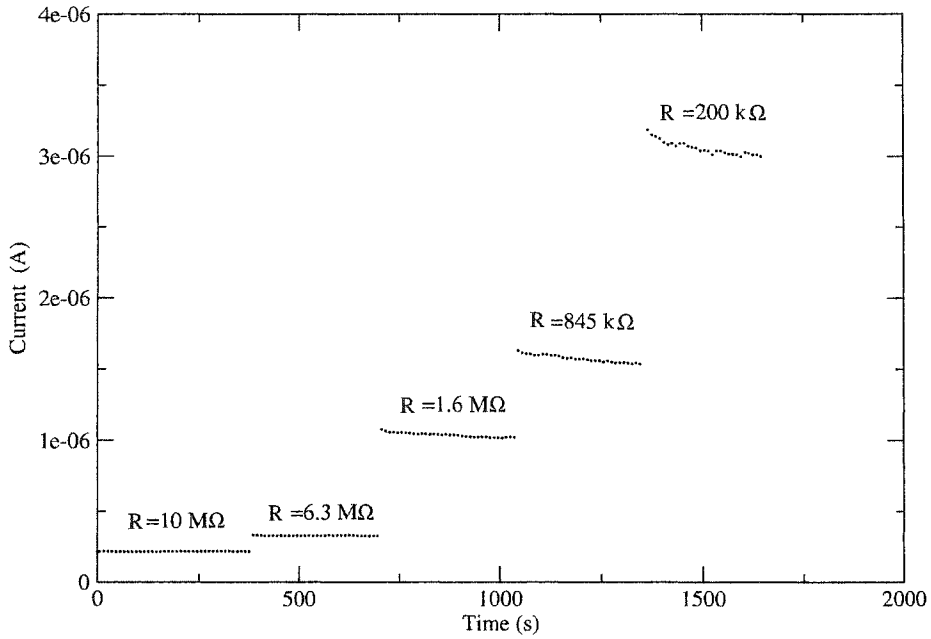

Figure 3.4: Typical current versus time curve with different loadings

potential:

$$\frac{1}{\zeta} = -\frac{I_p^*(0)\epsilon\pi a^2}{\nu\rho_d}\left[1 - \frac{2}{j\kappa a}\frac{J_1(j\kappa a)}{J_0(j\kappa a)}\right] \tag{3.38}$$

It should be noted that Eq. (3.38) is accurate for any κa providing that the zeta potential is less than 25 mV [24]. Generally, the zeta potential of ceramic on pure water is on the order of 10–30 mV [59, 80]. Thus, one can safely employ Eq. (3.38) to calculate the zeta potential of ceramics in the experiments and the results are shown in Table 3.2.

Our data agree reasonably well with published data [59, 80] for larger κa. However, the zeta potential for the filter with smaller κa (sample 4) was much smaller than expected.

As pointed out earlier, Eq. (3.35) predicts a linear relationship between U_L and I_L. However, the experimental measurements indicate different behavior for different pore size filters. Figure 3.5 shows the measured and predicted U_L -I_L curves

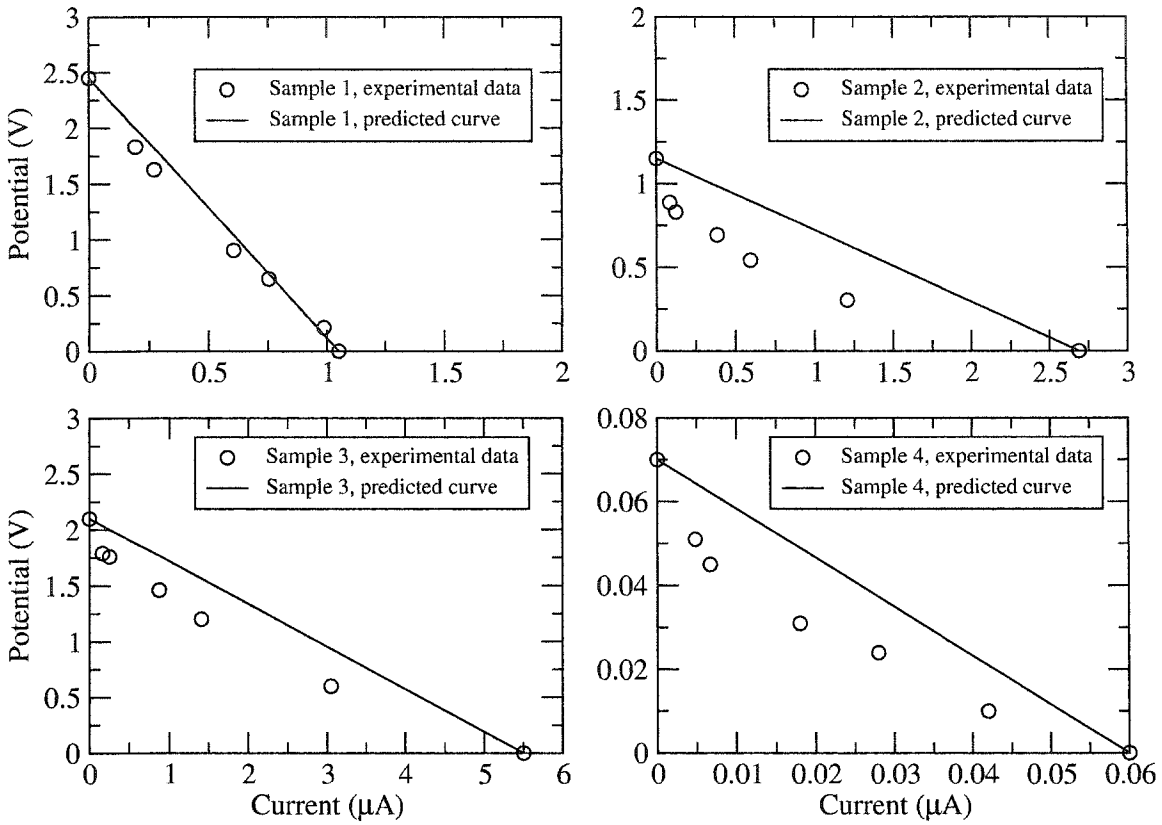

Figure 3.5: The measured and predicted U_L -I_L curves for different pore size filters

for different pore size filters. The measured curve was quite linear and agreed well with the predicted curve for the 6 micron filter (sample 1). However, the measured curves for the 2.5 micron (sample 2 and sample 3) and 0.16 micron (sample 4) filters were nonlinear and deviated from the predicted curves . The error may be caused by two reasons: one is the Debye-Hückel approximation, the other is the assumpsion that EDL is the same in all the cases. Since the Debye-Hückel approximation is in good agreement with the exact solution for low zeta potential, the error caused by the approximation can be safely neglected. As discussed in Chapter 2, the streaming potential is caused by the accumulation of ions downstream. When R_L is changed, the potential drop along the filter will change. If one assumes that the velocity profile, liquid and solid property such as conductivity, zeta potential, viscosity do not change,

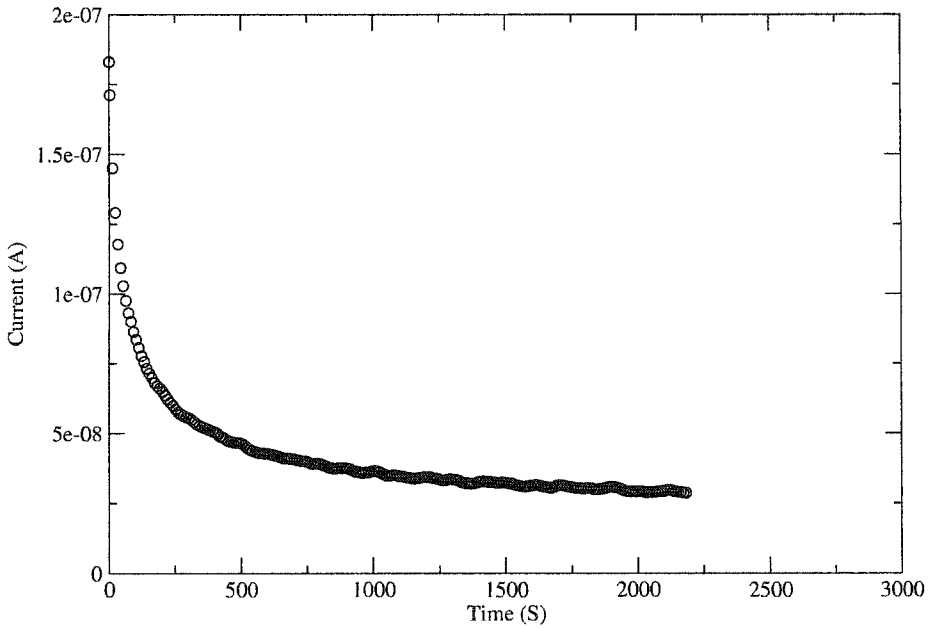

Figure 3.6: The streaming current versus time when the measurement was switched from streaming potential mode to streaming current mode for filter sample 4 with a flow rate 15 ml/hr.

the variation of the potential drop has to be caused by the redistribution of ions. In streaming potential mode, sufficient ions are required to accumulate downstream in order to provide the potential drop. When the resistor is switched to a lower value, it will require less ion accumulation downstream to provide smaller potential drop and vice versa. This is illustrated by the information demonstrated in Figures 3.6 and 3.7.

Figure 3.6 demonstrates that the measured streaming current decreases to a stable value when the measurement was suddenly switched from streaming potential mode to streaming current mode. When the measurement was switched from streaming potential mode to streaming current mode, the movement of the accumulated ions would cause the largest streaming current at the beginning. When the accumulated ions disappear gradually, the streaming current becomes smaller until a new equilibrium is established. On the other hand, Figure 3.7 indicates that the ions which provided the potential drop were accumulated gradually when the measurement was

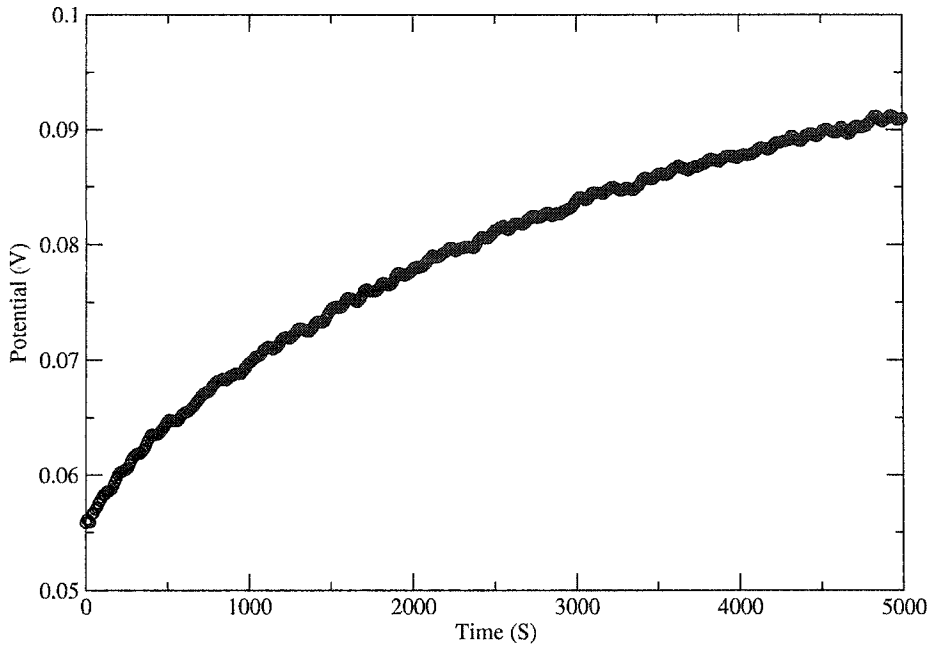

Figure 3.7: The streaming potential versus time when the measurement was switched from streaming current mode to streaming potential mode for filter sample 4 with a flow rate 15 ml/hr.

suddenly switched from streaming current mode to streaming potential mode. As a result, the ions in EDL would redistribute when the external resistance is changed. This redistribution of ions results from the fact that α and β in Eq. (3.35) were not constant. The change of α and β may be neglected in thin Debye layer and not for thick one. Therefore, nonlinearity of the U_L - I_L curve is caused by ion redistribution (EDL structural change).

3.6 Conclusions

The pressure-driven electrokinetic flow with an external load in porous media is studied in this Chapter. With the introduction of an external circuit, the ions in the EDL will redistribute. In thin Debye layer case, the predicted potential drop and current are in excellent agreement with the experiment data, which suggests that ion redistribution could be safely neglected. In thick Debye layer case, the poor agreement

indicates that ion redistribution has to be considered.

Chapter 4

Electrokinetic (EK) Generation

4.1 Introduction

The conversion of energy from one form to another, or the production of useful work, has long been an important element of engineering and scientific research. The larger goals of research into energy-based systems have been to further develop the technology, better understand any fundamental processes and improve efficiencies. Chemical energy, for example, can be readily converted into mechanical work by classical devices such as internal combustion and steam engines. Similarly, the potential energy of dammed water, and its associated hydrostatic pressure, can be exploited by turbines to be another source of mechanical work. If necessary, electric generators could be employed to convert any produced mechanical work into electrical work. Batteries and fuel cells are devices that avoid the creation of mechanical work and directly convert chemical energy into electrical work. This Chapter presents a novel approach and device that is part of this same broad family of energy-based systems, but uses the interactions between electrokinetics and microfluidics to directly convert the hydrostatic pressure of a liquid into electrical work. Since the energy source for this device is the coupling between electrokinetics and hydrodynamics, it is referred to as an electrokinetic (EK) power generation. This Chapter will describe the experimental results for electrokinetic power generation as a battery as the energy is stored within the potential energy of water.

Electrokinetic microfluidic behavior can be complicated and details can be found elsewhere [24, 25, 81, 82, 71, 83, 84, 85, 86, 87, 88]. As discussed earlier, liquid flow through a microchannel by means of an external pressure gradient can result in a convection current, known as the streaming current, and a streaming potential between two ends of microchannels due to the accumulation of ions or charges. The streaming current is typically on the order of nano amphere per kPa of pressure drop in a single microchannel. Though this magnitude is small, a method to enlarge such a current is proposed here. If more than one microchannels are assembled in parallel, the streaming currents are indeed additive and can be significant. With current fabrication technology, it is possible to assemble an array of microchannels with a large surface area to volume ratio. The larger this ratio, the more the movable ions and hence a larger streaming current can result. Alternatively, the requirement of a complex micro/nano-fabrication can be eliminated by using natural porous materials or readily available porous membranes. It is proposed here the concept of an electrokinetic battery by means of electrokinetic power generation which consists of an array of microchannels.

4.2 Natural electrokinetic battery

In reality, porous materials, such as glass filter, membrane, rock, and soil, could be considered as a natural electrokinetic battery. The use of natural materials avoids complex micro/nanofabrication procedures to produce microchannel arrays with a large surface area to volume ratio. In addition, natural porous material can have a high porosity ratio up to 60%. To explore this, a water battery system is constructed and shown in Figure 4.1. A simple syringe is used to drive water into a ceramic filter (Small Parts Inc. and Soilmoisture Equipment Corp.) and the two ends are connected by an electrometer (Keithley 6517A, Keithley Instruments). The two electrodes consisting of a silver meshed network were placed at the two ends of the ceramic rod and

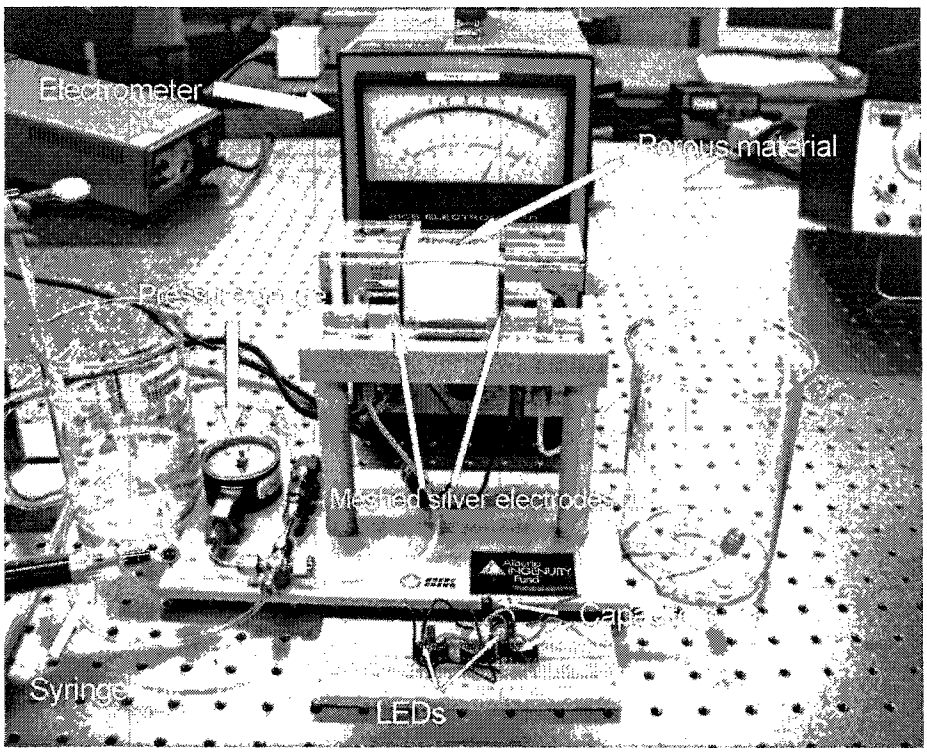

Figure 4.1: A picture of an electrokinetic battery system

in connection with the electrometer. All other connections are plastic or Teflon in order to minimize the influence of conductivity on the potential. The electrical energy is collected by means of two 100 μF capacitors which are alternatively charged and discharged for two LEDs (Figure 4.2). Deionized ultrafiltered (DIUF) water (Fisher Scientific) having a conductivity of 1.0 $\times 10^{-4}$ S/m was used as the testing liquid. Water was selected here because of its simplicity. Pushing the syringe by hand, a streaming potential of over 20 V and a streaming current of over 20 μA can be easily obtained. After about 8 seconds, the two LEDs light-up alternatively in every 10–12 seconds, depending on the input pressure.

In order to examine the efficiency of the EK battery, an automatic syringe pump was employed which provides a constant flow rate of DIUF water through the porous ceramic filter. The ceramic filters and experimental setup employed are the same as

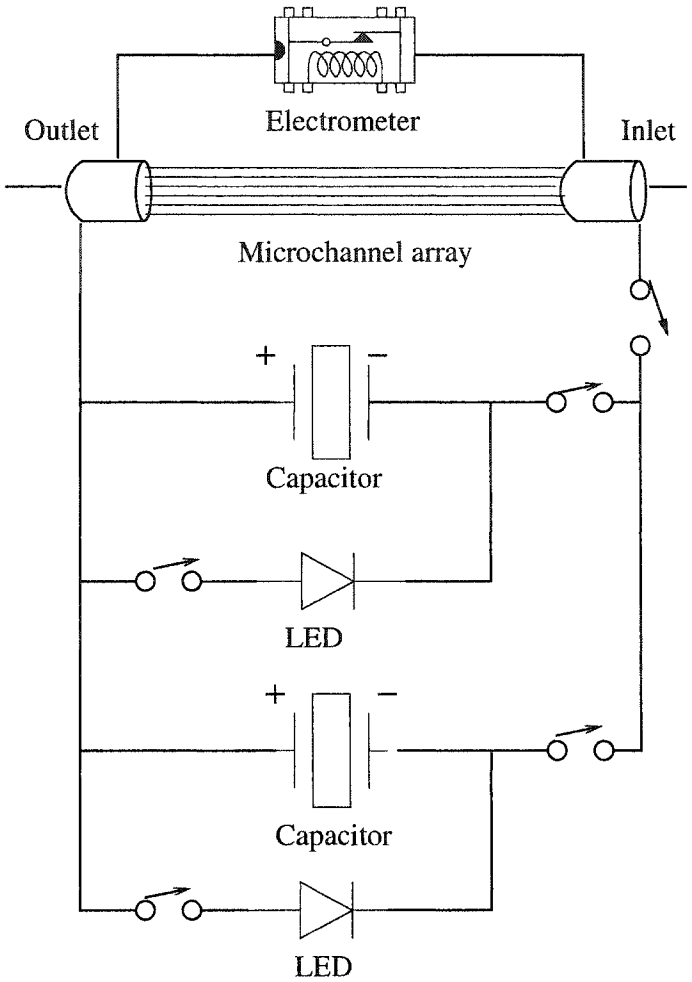

Figure 4.2: A schematic of an electrokinetic microchannel battery utilizing two capacitors and two LEDs

those used in Chapter 3. Consider a EK battery with an external circuit (see figure 3.1). The EK battery efficiency η_b is defined as the ratio of electrical power on the load to mechanical hydraulic power:

$$\eta_b = \frac{U_L I_L}{q\Delta P} \tag{4.1}$$

where ΔP is the pressure difference across the channels and q is the flow rate. It is noted that in the thin Debye layer limit, the electroviscous effect is negligible. If the flow rate is fixed, the pressure difference and the streaming current will be fixed for

Table 4.1: The maximum efficiency for different pore size filter

Sample	Maximum pore size (μm)	Maximum efficiency (%)
1	6	0.0176
2	2.5	7.04e-3
3	2.5	0.0224
4	0.16	2.32e-5

a given geometry. Table 4.1 shows the maximum battery efficiency for different pore size filters. When the pore size decreases, the efficiency decreases. The efficiency of filters with the same dimension and pore size but produced by different companies indicate different efficiencies and may be caused by the difference in material property.

Figure 4.3 demonstrates the U_L - I_L relationship for sample 1. By repeat pumping and draining the water, the streaming potential and streaming current increase to a limit at the same flow rate. This phenomenon was highly reproducible for all the filters studied. The role of impurities have been checked very carefully and ruled out its possibility; the presence of impurities would actually decrease the streaming potential instead of the observed trend. This above phenomenon is particularly intriguing as one can increase the streaming potential and current without increasing its pressure gradient. These procedures are described below as a mobile-ion-drain method.

As shown schematically in Figure 4.4a, water is initially stationary with respect to the channel walls and ions distribute themselves due to a charged surface. Water is then forced into the channel (Figure 4.4b), causing a stable potential difference across the two ends due to accumulation of the mobile ions downstream. When pumping is stopped (water is stationary), some of the mobile (counter) ions previously at the downstream had escaped by following the stream of water. Figure 4.4c illustrates this schematically by losing four counter ions. Here, the system is in deficit of four counter ions and the only way to recover equilibrium is to obtain them from the surface by dissociation. Thus, the system will reach another equilibrium by dissociation, result-

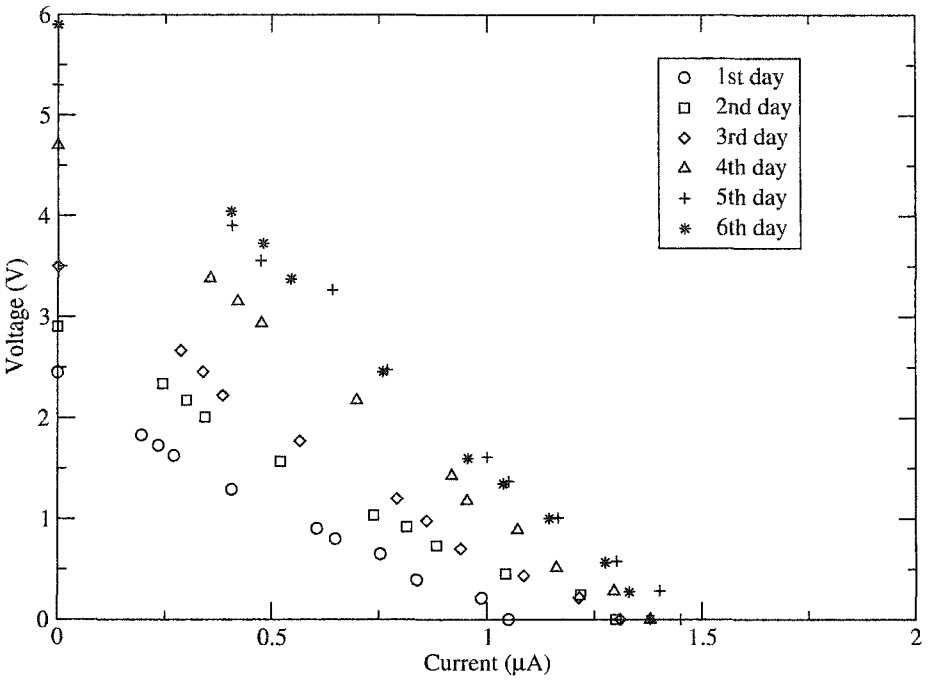

Figure 4.3: U_L-I_L relationship for pore size 6 micron filter

ing in a more negatively charged surface. This is further supported by experimental evidence that a small negative potential exists even when there is no flow; that is, the system has become negatively charged. When pumping resumes (Figure 4.4d), there will be more mobile ions due to the increase in surface charge density and hence a higher streaming potential will result. Figure 4.5 demonstrates the mobile-ion-drain effect on the efficiency of a 1.6 MΩ loading for different pore size filters. All the filters which have different pore sizes and come from different companies show the same behavior: the efficiency increases to a limit by pumping and draining the water repeatedly. For a six-day period, the efficiency improvement are 162.5%, 31.8% and 45.98% for filters with maximum pore size 6 μm (sample 1), 2.5 μm (sample 3) and 0.16 μm (sample 4) respectively.

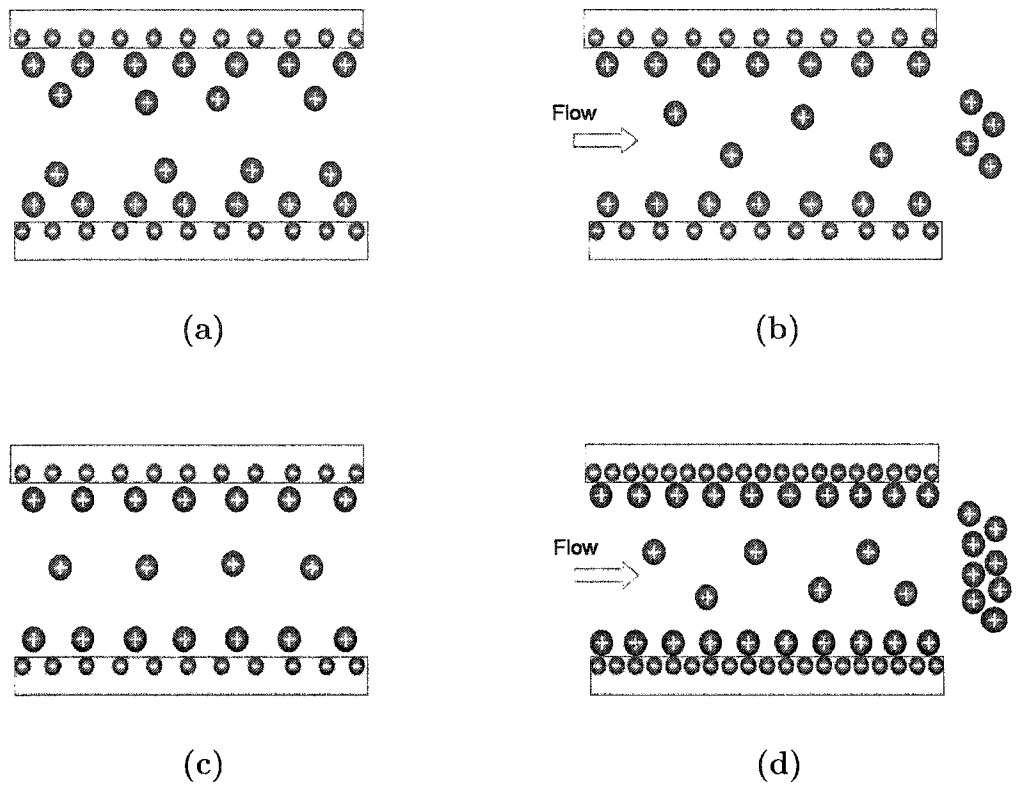

Figure 4.4: A schematic of the mobile-ion-drain method. (a) Surface has adopted a charge when in contact with water and EDL forms; (b) A stable streaming potential exists due to the water flow and accumulation of mobile ions; (c) The mobile ions in (b) have been drained and the surface will disassociate and become negatively charged; (d) The surface has become more negatively charged when flow resumes, resulting in a larger streaming potential.

4.3 Conclusions

In summary, a new method is proposed to generate electricity by charge separation through direct conversion of motion of a fluid (water) to electricity. A mobile-ion-drain method has also been demonstrated to increase the efficiency of the EK battery without increasing pressure drop. The water battery demonstrated here is environmentally friendly, with no emission and moving parts.

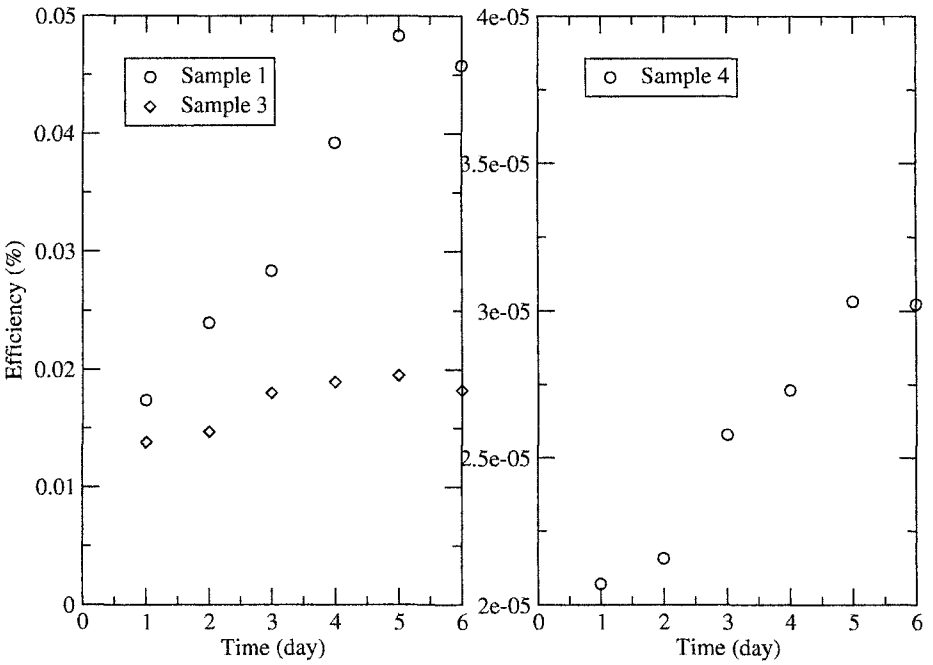

Figure 4.5: Ion-drain effect on the EK battery efficiency

Chapter 5

A promising slip coating: Self-Assembled Monolayers (SAMs) and experiments

5.1 Introduction

A recent advance in the fabrication of nanoscale coatings is the use of the so-called Self-Assembled Monolayers (SAMs) [89, 90, 91, 92]. These films are two-dimensional organic assemblies that form by the spontaneous adsorption of functionalized, long-chain molecules onto metal or metal oxide supports. They provide models to systematically study a wide range of interfacial/surface phenomena. The organic and biological properties of these films are largely controlled by the end groups of the molecules and can be manipulated by tailoring the end functional groups. SAMs are of technical interest for the fabrication of sensors, protective layers, for lubrication, and as patternable materials [93]. They provide a pathway for a better understanding of many technological systems where interfacial events play a dominant role.

The history of SAMs can be traced to the earlier papers of Zisman *et al.* [94]. where glass surfaces were exposed to dilute solutions of long-chained alcohols in hexadecane. Oriented monolayer films were then formed on the substrate that were not wetted by the solvent. Zisman et al. further studied various surfactant-like molecules including long-chained amines, carboxylic acids and amides on metal and metal oxide surfaces [95, 96]. The systems considered by Zisman et al. exhibit only modest stabilities and were limited only to low-energy hydrophobic surfaces. Nuzzo *et al.*

[97] later extended Zisman's approach by relying on a stronger and specific interactions between sulfur and gold for molecular self-assembly. The specific interaction between gold and sulfur allows adsorption of thiols not only onto gold, but also other surfaces such as silver, copper and mercury. The mechanism of such self-assembly originated from a large interfacial driving energy when the metal substrates are reduced. This specific adsorption is stronger than the molecular film formed by the Langmuir-Blodgett technique which relies on packing of molecules and subsequently transfer to surfaces. Among the metals for self-assembly, self-assembled monolayers (SAMs) derived from the adsorption of organothiols onto gold have been extensively investigated for studying their potential uses as corrosion inhibitors, resist layers, components of chemical sensors, and models for organic and biological surfaces.

As a nanoscale coating on MEMS devices, SAMs exhibit many advantages: ease of preparation, density of defects low enough to be useful in many applications, amenability to controlling interfacial properties (physical, chemical, electrochemical and biochemical) [93], very thin thickness at the order of nanometers. Comparing with the thickness of traditional polymer coating at the order of μm, SAMs is certainly the best choice to control interface/surface properties of microchannels.

5.2 Effect of nano-crystalline on hydrophobicity of SAMs

SAMs is a single layer of long-chain molecules. Intuitively, properties of SAMs coatings should be determined by the exposed end functional groups. However, formation of SAMs are influenced by the nanostructure of solid substrates and process of adsorption. In this section, effects of nano-crystalline of substrates on hydrophobicity of SAMs will be studied by means of contact angle , Ellipsometry, Fourier Transform Infrared Spectroscopy (FTIR) and the Atomic Force Microscopy (AFM) measurement.

5.2.1 Experimental section

5.2.1.1 Materials.

Silicon wafers of test grade were obtained from Wafer World (West Palm Beach, FL) in circular discs of about 10 cm diameter and were cut into rectangular shapes of about 2.5 cm $\times$ 5 cm. Gold shot (99.999%) and titanium shot (99.995%) were obtained from Kurt J. Lesker (Clairton, PA). Ethanol (100%) was obtained from the Chemistry Dept. at the University of Alberta. Octadecanethiol [$CH_3(CH_2)_{17}SH$] was obtained from Aldrich and used as received. Six liquids were chosen for contact angle measurements. Selection was based on the following criteria: (1) they should include a wide range of intermolecular forces; (2) they should be non-toxic; and (3) the liquid surface tension should be higher than the anticipated solid surface tension [98]. They are listed in Table 5.1.

5.2.1.2 Preparation of SAMs.

Supported gold films were prepared by sequentially evaporating titanium ($\sim$ 10 nm) and gold ($\sim$ 100 nm) onto small rectangular silicon wafers in a diffusion-pumped vacuum chamber at $\sim 10^{-6}$ torr. The chamber was backfilled with air and the substrates were used within 48 h of preparation. The evaporated surfaces were rinsed with ethanol before SAMs formation. SAMs were prepared by immersing into 1 mM of $CH_3(CH_2)_{17}SH$ in ethanol overnight. The resulting surfaces were rinsed with ethanol and blown dry by nitrogen before use. Evaporated gold substrates were also flame annealed for $\sim$ 30 s using a bunsen burner under ambient laboratory condition. After $\sim$ 1 minute, the annealed substrate was then immersed into 1 mM of $CH_3(CH_2)_{17}SH$ in ethanol overnight.

5.2.1.3 Characterization of SAMs.

SAMs were first characterized by a Sopra GES5 Variable Angle Spectroscopic Ellipsometer. The ellipsometry measurements were performed using a rotating polarizer in the tracking analyzer mode. A broad band of light (300 to 850 nm) from a 75 W Xe-arc lamp is linearly polarized and directed onto the film surface at an incident angle of 75° from the surface normal. Each bare gold substrate were measured by the ellipsometer as references immediately after evaporation. After immersion into 1 mM of octadecanethiol/ethanol solution overnight, a new set of data for each substrate were measured again using an ambient-film-substrate model for regression with known refractive index (n and k) for octadecanethiol absorbed onto gold. The refractive index for octadecanethiol absorbed onto gold as a function of wavelength was independently obtained from a Sopra GXR Grazing X-ray Reflectometer, rather than assuming an index of refraction at a given wavelength as typically performed in the literature. Such spectroscopic measurements are expected to provide more accurate results in ellipsometer thickness since the optical constants for a range of wavelengths were used simultaneously.

Reflectance Infrared spectra of SAM of octadecanethiol onto Au were obtained using a ThermoNicolet Nexus 670 spectrometer equipped with a VeeMax glazing angle accessory. A p-polarized light was incident at 70° from the surface normal and the reflected light was detected by means of a MCT-A detector cooled with liquid nitrogen. The spectra resolution was 2 cm^{-1}. Spectra were referenced to the corresponding bare (anneal and non-annealed) Au substrates and 1024 scans were obtained for good signal-to-noise ratios. An infrared gain of 2 was selected for all reflectance infrared (IR) measurements to ensure that the input IR signals are constant. Samples were rinsed with ethanol and blown dry by N_2 prior to characterization.

The atomic force Microscopy (AFM) measurements were performed using a Digital

Instruments Nanoscope IIIa atomic force microscope (Digital Instruments, Santa Barbara, CA). Standard silicon nitride cantilevered probes were used with a force/spring constant in the range between 0.06 – 0.58 N/m. The AFM images of annealed and non-annealed Au surfaces were captured by using contact mode under ambient laboratory conditions. The surfaces were cut into 1 cm × 1 cm samples to fit onto a 1.5 cm × 1.5 cm sample stage.

5.2.1.4 Contact Angle Measurements

Contact angle measurements were chosen as the last step for the characterization of SAMs. A Linux version of the Axisymmetric drop shape analysis - profile (ADSA-P) was used for sessile drop contact angle measurements. ADSA-P is a technique to determine liquid-fluid interfacial tensions and contact angles from the shape of axisymmetric menisci, i.e., from sessile as well as pendant drops [99, 100]. Assuming that the experimental drop is Laplacian and axisymmetric, ADSA-P finds a theoretical profile that best matches the drop profile extracted from an image of a real drop, from which the surface tension, contact angle, drop volume, surface area and three-phase contact radius can be computed. The strategy employed is to fit the shape of an experimental drop to a theoretical drop profile according to the Laplace equation of capillarity, using surface/interfacial tension as an adjustable parameter. The best fit identifies the correct surface/interfacial tension from which the contact angle can be determined by a numerical integration of the Laplace equation. Details of the methodology and experimental set-up can be found elsewhere [99, 100, 101, 102, 103].

Sessile drop experiments were performed by ADSA-P to determine the advancing and receding contact angles. The temperature and relative humidity were maintained, respectively, at 23.0 ± 0.5°C and at about 40%, by means of an independent central air-conditioning unit in the laboratory. It has been found that, since ADSA-P assumes an axisymmetric drop shape, the values of liquid surface tensions measured

Table 5.1: Experimental advancing and receding contact angles on SAMs of octadecanethiol $CH_3(CH_2)_{17}SH$ absorbed onto Au. Error bars are the 95% confidence limits.

liquid	γ_{lv} (mJ/m^2)	θ_a (deg.)	θ_r (deg.)
water	72.70 ± 0.09	119.1 ± 0.8	100.2 ± 0.7
formamide	59.08 ± 0.01	88.7 ± 0.8	63.0 ± 1.4
ethylene glycol	47.55 ± 0.02	81.5 ± 0.6	66.4 ± 1.1
bromonaphthalene	44.31 ± 0.05	67.2 ± 0.8	44.1 ± 0.8
decanol	28.99 ± 0.01	50.7 ± 0.5	38.2 ± 1.1
hexadecane	27.62 ± 0.01	45.4 ± 0.4	< 20.0

from sessile drops are very sensitive to even a very small amount of surface imperfection, such as roughness and heterogeneity, while contact angles are less sensitive. Therefore, the liquid surface tensions used in this study were independently measured by applying ADSA-P to a pendant drop, since the axisymmetry of the drop is enforced by using a circular capillary. Results of the liquid surface tension from previous studies [101, 104, 105] are reproduced in Table 5.1.

In this study, at least 5 and up to 15 dynamic contact angle measurements at velocities of the three-phase contact line in the range from 0.1 to 1.0 mm/min were performed for each liquid. The choice of this velocity range was based on previous studies [101, 102, 106] which showed that low-rate dynamic contact angles at these velocities were essentially identical to the static contact angles, for these relatively smooth surfaces. Liquids were supplied from below the surface through a hole of $\sim$ 1 mm in diameter on the substrate by means of a motorized-syringe system. Details of this setup can be found elsewhere [101, 102].

5.2.2 Results and discussion

5.2.2.1 Formation of SAMs on polycrystalline gold

Figure 5.1 displays a typical low-rate dynamic contact angles of water on SAM of octadecanethiol $CH_3(CH_2)_{17}SH$ absorbed onto Au. As can be seen, increasing the drop volume V linearly from 0.11 cm^3 to 0.12 cm^3 increases the apparent contact

angle θ from 110 to 118° at essentially constant three-phase contact radius R. This is due to the fact that even carefully putting an initial water drop from above on a solid surface can result in a contact angle somewhere between advancing and receding. Further increase in the drop volume causes the three-phase contact line to advance, with θ essentially constant as R increases. Increasing the drop volume in this manner ensures the measured θ to be an advancing contact angle. Since the contact angles are essentially constant after $R = 0.37$ cm and according to [102], these contact angles can be used for the determination of solid surface tensions. The averaged contact angle of 118° in Figure 5.1 is consistent with the literature values [107, 108]. The experimental results for the other five liquids also yield essentially constant contact angles; these results together with the receding angles are summarized in Table 5.1. The solid-liquid work of adhesion W_{sl}, $\cos\theta$ and $\gamma_{lv}\cos\theta$ versus γ_{lv} for these liquids are plotted in Figure 5.2. However, there are significant scatters in these data even though the procedures of low-rate dynamic contact angles were used to distinguish meaningful angles from meaningless ones.

From the point of view of surface energetics, it should be noted that a water contact angle of 119.1° (Table 5.1) for a surface exposing purely methyl groups [$CH_3(CH_2)_{17}S$/Au] appears to be too high. For example, the experimental advancing contact angles of water on polystyrene, hexatriacontane, Teflon PTFE, and fluorocarbon are expected to be, respectively, 90–92°, 105–107°, 108–110°, and 118–120°, as summarized in Table 5.2. This comparison suggests that SAMs of octadecanethiol absorbed onto Au which are supposed to expose mainly methyl groups should have a solid surface tension similar to that of fluorocarbon (118–120°) and lower than that of Teflon PTFE (108–110°). These interpretations are questionable. From a surface energetic viewpoint, if SAM of octadecanethiol absorbed onto Au exposes only methyl group, it is expected that the SAM surface behaves very much like a hexatriacontane surface (with water advancing angles between 105–107°) since both surfaces have pre-

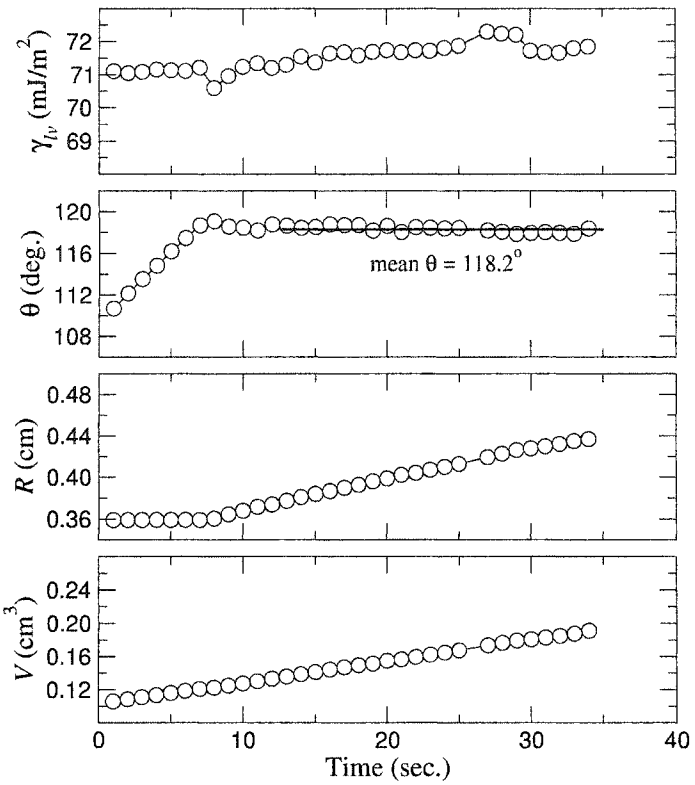

Figure 5.1: Low-rate dynamic contact angles of water on SAMs of octadecanethiol $CH_3(CH_2)_{17}SH$ absorbed onto gold.

dominately methyl groups exposed to the surface. The only apparent difference is that the former is a monolayer and the latter is a thick crystalline and well-order surface. The hexatriacontane surface was prepared by vapor deposition of which the surface quality was so good that there was no contact angle hysteresis for water [109]. SAMs with methyl groups cannot possibly have a solid surface tension as low as that of fluorocarbon. The contact angle data of octadecanethiol SAM/Au were superimposed onto those of the hexatriacontane in Figure 5.2 and found that the monolayer data appear to fluctuate around those of the hexatriacontane. It should be noted that conventional thinking regarding contact angles is that they are indicators for surface hydrophobicity in terms of solid surface tensions; for example, higher contact angle implies lower surface energy and similarly lower contact angle suggests higher surface

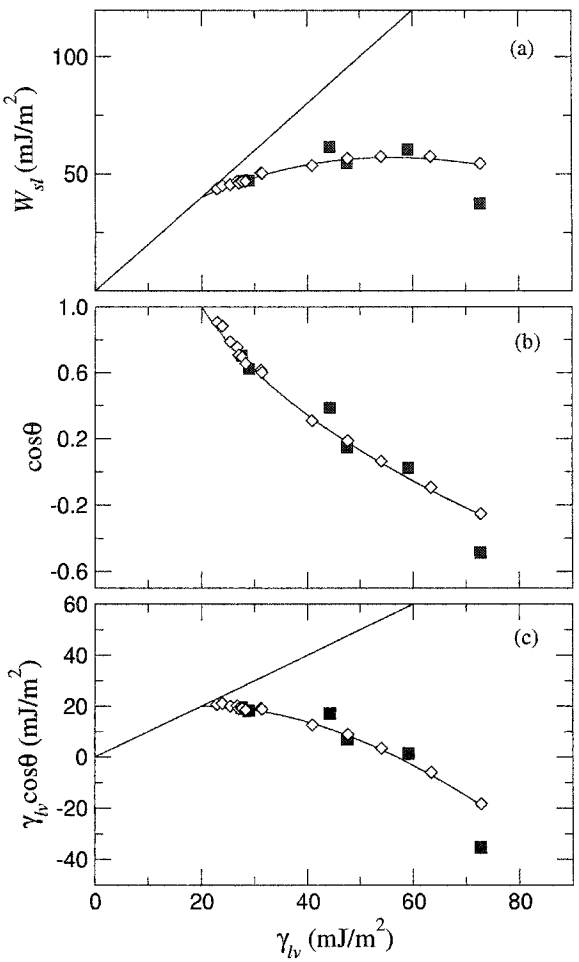

Figure 5.2: (a) The solid-liquid work of adhesion W_{sl}, (b) cosine of the contact angle $\cos\theta$ and (c) liquid vapor surface tension times cosine of the contact angle $\gamma_{lv}\cos\theta$ versus the liquid-vapor surface tension γ_{lv} for hexatriacontane (Diamonds) and SAMs of octadecanethiol $CH_3(CH_2)_{17}SH$ absorbed onto gold (Black squares).

energy. Such an interpretation is not necessarily conclusive for the systems considered here as will be illustrated and discussed later. It is speculated that the discrepancy may come from additional and unexpected effect(s) of changing solid-liquid interfacial tensions on the contact angles through the variation of surface structures, even though the solid-vapor surface tension might have been constant. If γ_{sv} and γ_{lv} are constant, changes in θ suggest that γ_{sl} is changing. In the next section, such effects will be quantified by looking into the surface structures of octadecanethiol SAMs

Table 5.2: Comparison of expected water contact angles on fluorocarbons, PTFE, polystyrene (PS) and poly(methyl methacrylate) (PMMA) with that measured on SAMs of octadecanethiol $CH_3(CH_2)_{17}SH$ absorbed onto gold.

Surface	Water contact angle (deg.)
Fluorocarbon	118 – 120
PTFE	108 – 110
Hexatriacontane	105 – 107
Polystyrene, PS	90 – 92
Poly(methyl methacrylate), PMMA	73 – 75
$CH_3(CH_2)_{17}S$/Au	118 – 120

absorbed onto Au.

It is commonly known in the literature [97, 110] that thermally evaporated gold yields smoother and better polycrystalline structures than that by sputtering. It has also been found that SAMs on thermally annealed gold have larger terraces with less surface defects [111, 112]. Thus, SAMs on annealed gold are typically used in Atomic Force Microscopy (AFM) study to obtain atomic resolution pictures. As a matter of fact, most contact angle studies of SAMs on gold were prepared either by sputtering or thermal evaporation due to the relatively simple procedures [108, 113, 114, 115]. To our knowledge, no systematic contact angle study on SAMs has yet been performed and has looked into the details of how surface structures affect wetting in terms of surface energetic interpretation using thermally annealed gold. Thus, in the next section low-rate dynamic contact angles on octadecanethiol monolayers formed on thermally annealed gold will be investigated, in an attempt to isolate any (possible) effect of surface structures and defects on solid surface tension interpretation.

5.2.2.2 Formation of SAMs on annealed gold.

Figure 5.3 shows the low-rate dynamic contact angle results of water on SAMs of octadecanethiol absorbed onto a thermally-annealed-gold substrate. Similar to the experimental results in Figure 5.1, as V increases at the beginning, θ increases at

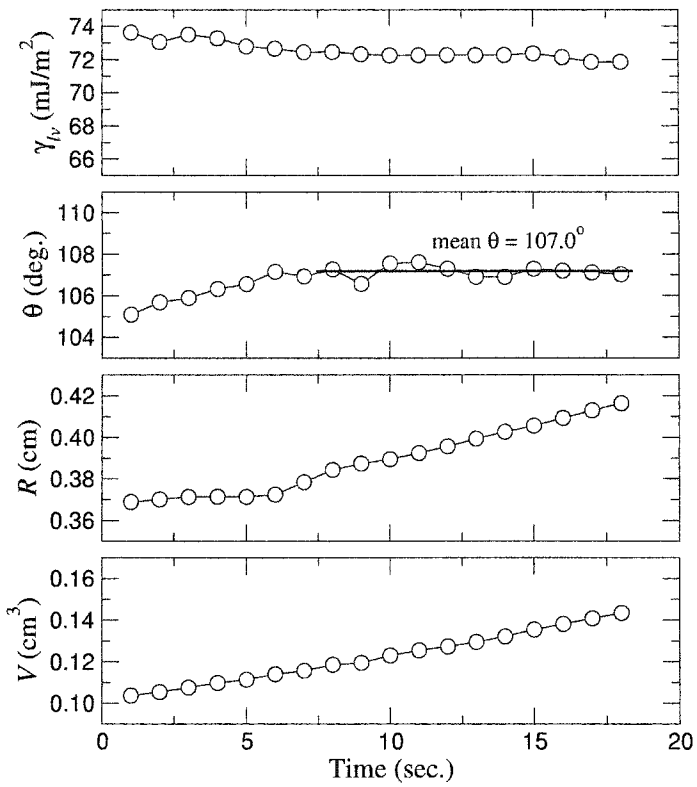

Figure 5.3: Low-rate dynamic contact angles of water on SAMs of octadecanethiol $CH_3(CH_2)_{17}SH$ absorbed onto annealed gold.

constant R. This is due to the fact that such contact angles are not truly advancing angles and it takes time for the drop front to advance. As V increases further, the three-phase contact radius R moves and the contact angle remains rather constant. Averaging the contact angle yields a mean value of 107.0°. It can be seen that this water contact angle value (107.0°) is significantly lower than that shown in Figure 5.1 (118.2°) on the evaporated (non-annealed) gold. It is also noted that the contact angle obtained here (107.0°) for the $CH_3(CH_2)_{17}S$/thermally-annealed-gold is similar to those obtained on the hexatriacontane (Table 5.2) and paraffin. This result agrees with the expectation that a monolayer surface exposing predominately methyl groups should have a similar solid surface tension and hence contact angle as those of hexatriacontane and paraffin surfaces. Low-rate dynamic contact angle measurements

Table 5.3: Experimental advancing and receding contact angles on SAMs of octadecanethiol $CH_3(CH_2)_{17}SH$ absorbed onto evaporated (non-annealed) and annealed gold. Error bars are the 95% confidence limits.

		Non-annealed		Annealed	
liquid	γ_{lv}	θ_a (deg.)	θ_r (deg.)	θ_a (deg.)	θ_r (deg.)
water	72.7	119.1 ± 0.8	100.2 ± 0.7	106.9 ± 0.5	92.3 ± 0.9
formamide	59.1	88.7 ± 0.8	63.0 ± 1.4	92.4 ± 1.5	69.2 ± 1.9
ethylene glycol	47.6	81.5 ± 0.6	66.4 ± 1.1	81.6 ± 2.4	68.2 ± 1.6
BN[a]	44.3	67.2 ± 0.8	44.1 ± 0.8	76.1 ± 0.9	64.3 ± 1.3
decanol	28.9	50.7 ± 0.5	38.2 ± 1.1	53.2 ± 0.9	45.1 ± 1.3
hexadecane	27.6	45.4 ± 0.4	< 20.0	45.7 ± 0.8	35.4 ± 2.2

[a] Bromonaphthalene

for the remaining five liquids were performed and found to be also constant. These angles, together with the receding angles, are summarized in Table 5.3.

5.2.2.3 Characterizations by Ellipsometry, FT-IR and AFM

The ellipsometer thickness for octadecanethiol $CH_3(CH_2)_{17}SH$ absorbed onto annealed gold was consistently 21Å; whereas that formed on the non-annealed Au varied between 20–21Å. While this difference is not statistically significant, it was noticed that the experimental $\tan\Psi$ and $\cos\Delta$ for the non-annealed-Au samples did not always match those of the theoretical curves. Nevertheless, our thicknesses are consistent with those reported in the literature [107].

The reflectance spectra for SAMs derived from octadecanethiol on Au and annealed-Au are shown in Figure 5.4. In the both spectra of Figure 5.4, the asymmetric methylene peaks appeared at ~ 2918 cm^{-1}. This indicates a primarily trans-zigzag extended hydrocarbon chain with few gauche conformers. Both spectra demonstrate that SAMs of octadecanethiol absorbed onto Au and annealed Au are highly crystalline. However, the intensities of the methylene peaks are larger on Au and smaller on the annealed Au. The difference in the peak intensity could reflect different canted orientations for the polymethylene chains on these surfaces or different amount of the

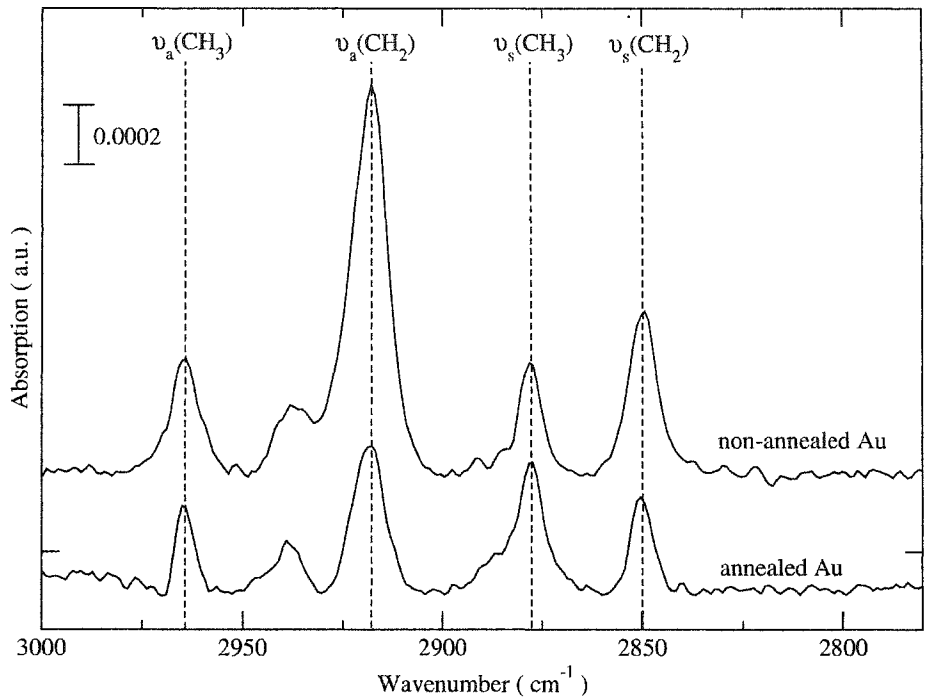

Figure 5.4: Grazing incidence polarized infrared spectra for SAMs of octadecanethiol $CH_3(CH_2)_{17}SH$ absorbed onto evaporated (non-annealed) and annealed gold. The approximate positions of the methylene modes are 2918 (asym) and 2850 (sym) cm^{-1}, and those for the methyl modes are 2964 (asym), 2935 (sym, Fermi resonance), and 2879 (sym) cm^{-1}. The spectra have been offset vertically for clarity.

polymethylene chains that the IR detected. Since the tilt of chain on the Au substrate for alkanethiolate SAMs is known to be $\sim 30°$ and this structural orientation is unlikely to be changed by annealing, it is speculated that the difference in the intensity of the asymmetric methylene peaks appear at ~ 2918 cm^{-1} and 2850 cm^{-1} indicates different amount of polymethylene chains that were detected by the IR. The spectrum for the adsorbed layer of octadecanethiol on non-annealed-Au exhibits a higher dichroic ratio (~ 2) for the methylene adsorption modes $[\nu_a(CH_2)/\nu_s(CH_2)]$; and that on the annealed-Au exhibits a much lower dichroic ratio (~ 1.3). It is also noted that the intensities of the methyl modes at 2964 (asym), 2935 (sym, Fermi resonance), and 2879 (sym) cm^{-1} for the two substrates in Figure 5.4 are similar. These features in the spectra provide evidence that SAM of octadecanethiol on the non-annealed Au

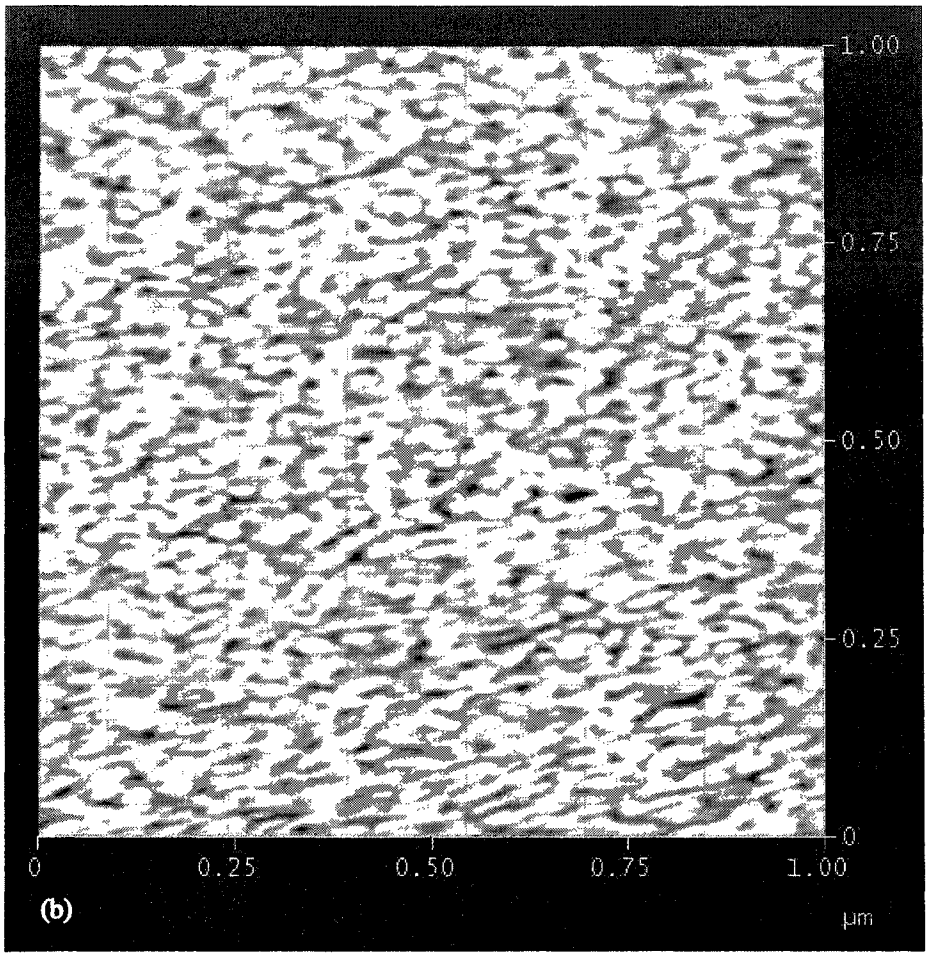

Figure 5.5: AFM images of non-annealed gold for a scan size of 1 μm.

has a structure that is not the same as that on the annealed Au.

Independent AFM images shown in Figure 5.5 and figure 5.6 suggest that the annealed Au has larger terraces [as much as 200 nm]; while that of the non-annealed Au has much smaller gold steps. From the interpretation of the above IR and AFM results, a model was constructed in Figure 5.7 that illustrates a possible arrangement of octadecanethiol absorbed onto non-annealed and annealed Au. From the schematic, it is expected that the reflectance IR would detect more methylenes per unit projected area on the non-annealed Au than that for the annealed Au. This is due to the polycrystallinity nature of non-annealed Au that causes variation of the methyl and

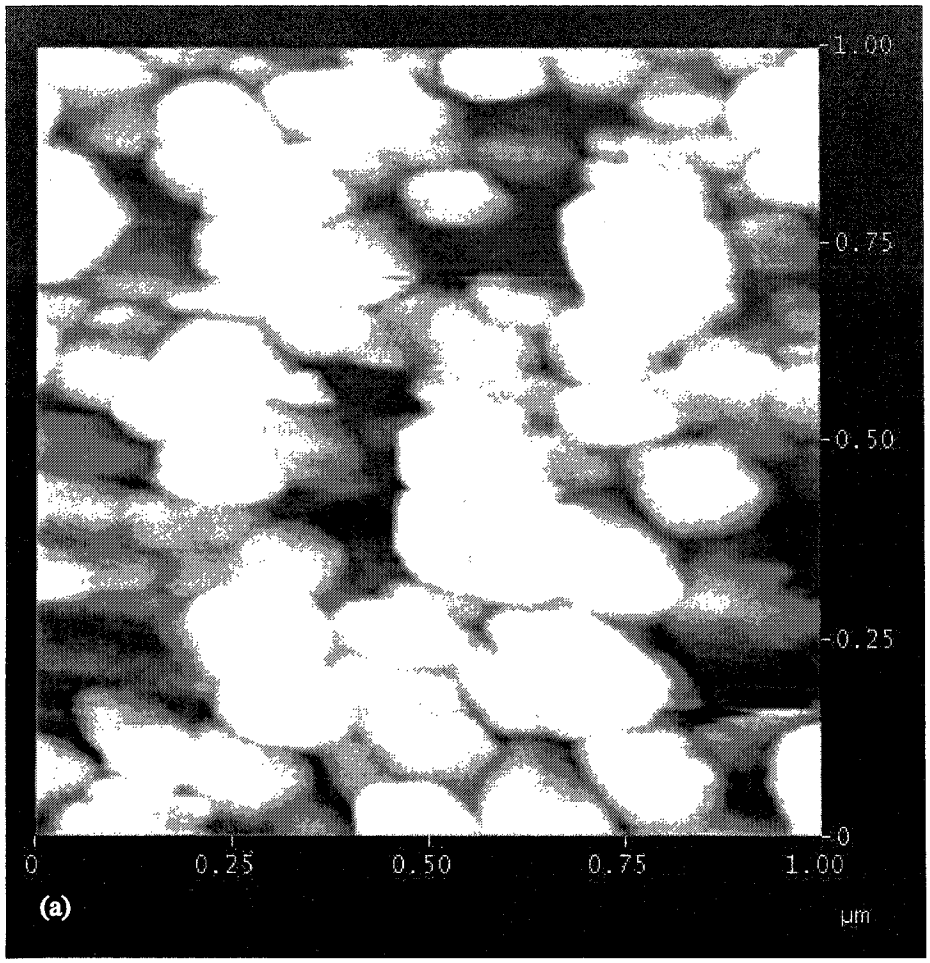

Figure 5.6: AFM images of annealed gold for a scan size of 1 μm.

methylene groups exposed to water. The schematic also supports the IR results that the intensities for the methyl adsorption peaks on both substrates should be similar, as the amount of methyl groups exposed to water per unit projected area would be more or less similar.

5.2.2.4 Wetting interpretation in terms of solid surface tensions

Contact angle interpretation requires extreme experimental care to ensure that all of the commonly accepted assumptions are not violated. It is apparent in Table 5.3 that, in general, the contact angle hysteresis $H = \theta_a - \theta_r$ decreases for the annealed gold substrate, suggesting better surface quality. The slightly larger errors for the

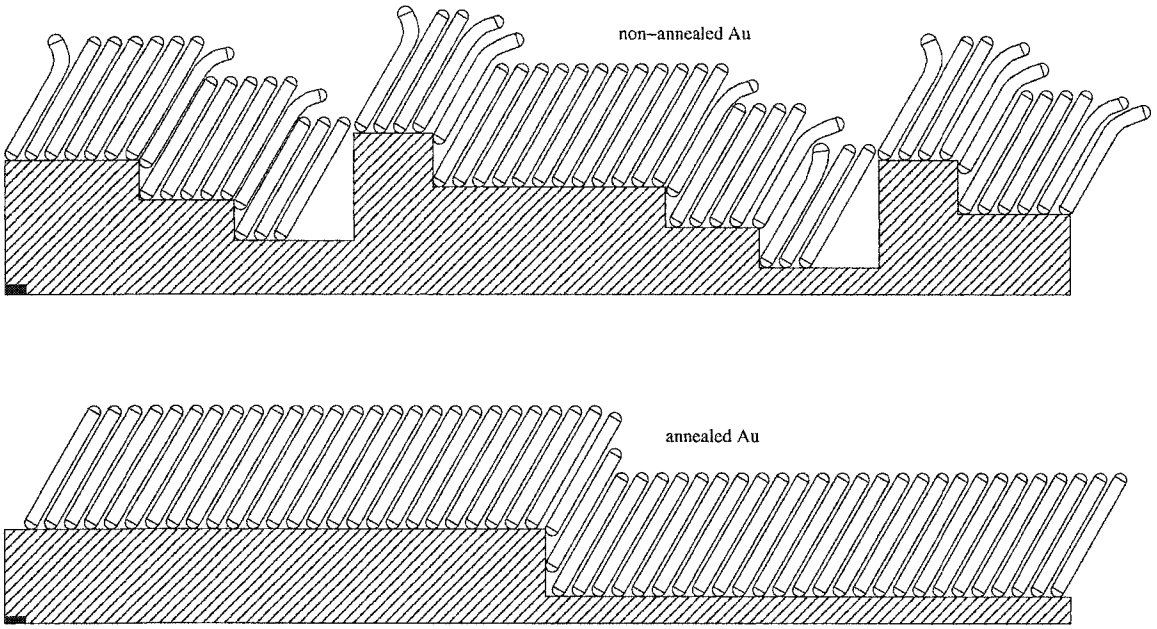

Figure 5.7: Schematic illustration of SAM assembly on two different Au substrates. The upper figure demonstrates SAM assembly of octadecanethiol absorbed onto non-annealed Au with smaller gold steps. The lower figure illustrates SAM assembly of octadecanethiol absorbed onto annealed Au with larger terraces.

contact angle data of octadecanethiol absorbed onto annealed Au were due to the variation of our annealing procedures. From the AFM results above, one may conclude that the non-annealed surface consists of smaller gold steps, whereas that of the annealed one has larger terraces and less defects, as illustrated schematically in Figure 5.7. In the case of the non-annealed samples, water could "see" deeper of the surface layer (the methylenes) under the methyl groups due to the relatively less packed monolayers as a result of smaller gold steps or defects. This allows formation of additional intermolecular interactions between water and the methylenes in the solid-liquid interface. In this case, the surface no longer consists of predominately methyl groups, but a mixture of methyl and methylene groups in the solid-liquid interfacial region. These molecular interactions with methylenes would result in a higher, additional, interfacial tension between the solid-liquid interface, $\Delta\gamma_{sl}$, and is illustrated schematically in Figure 5.8. This additional effect is believed to have less

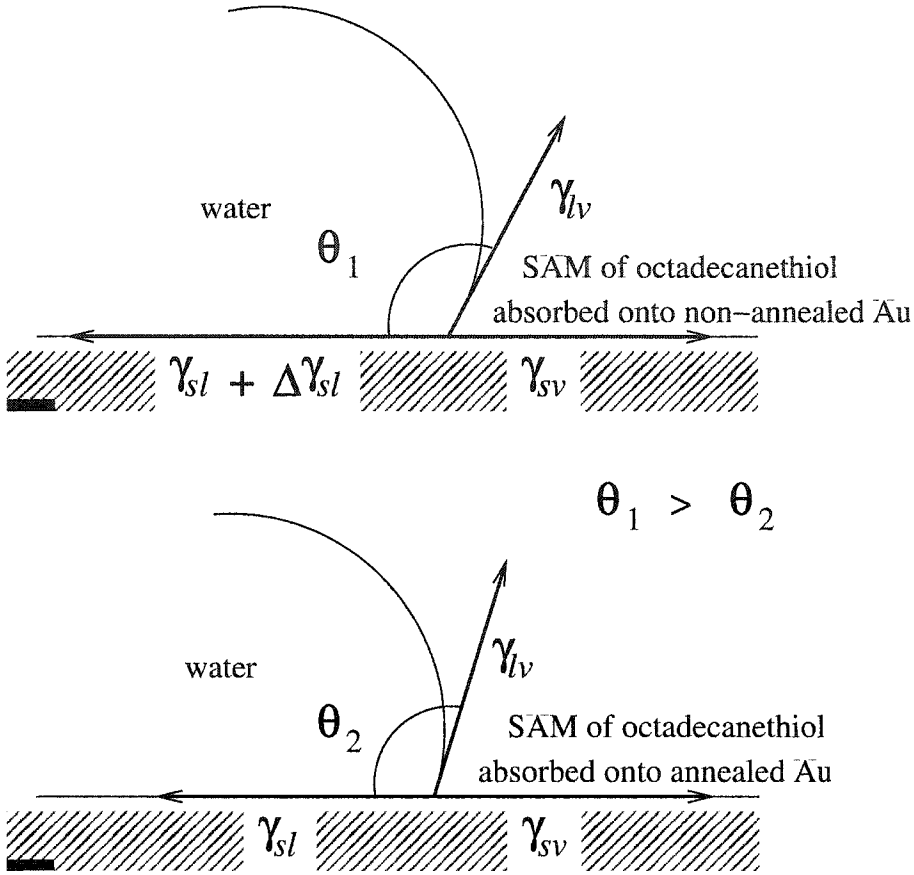

Figure 5.8: Schematic illustration of how the variation of surface structures affect the solid-liquid interfacial tension γ_{sl} for SAMs of octadecanethiol on non-annealed and annealed Au. $\Delta\gamma_{sl}$ in the upper figure represents the increase in the solid-liquid interfacial tension from that of an annealed Au. Given that the liquid-vapor interfacial tension γ_{lv} and the solid-vapor interfacial tension γ_{sv} remain unchanged, increase in $\Delta\gamma_{sl}$ results in a higher contact angle θ_1 than that of the annealed Au, θ_2.

influence on the solid-vapor interface due to presence of the relatively less densed water vapor on the solid-vapor interface. Assuming that γ_{sv} is roughly constant for both annealed and non-annealed surfaces, increase in γ_{sl} for the latter would cause the contact angle to increase from that of a surface where water can only "see" most of the outer methyl groups and less methylene groups. Thus, it appears that the change in the contact angle is a result of additional and unexpected formation of intermolecular interactions in the solid-liquid interface for less packed monolayers. The

magnitude would depend, of course, on the intermolecular strength, polarity of the liquid and structures of the monolayers. In this case, even though the substrate is apparently fixed, the intermolecular interactions would not be the same for a given pair of liquid and solid, depending on surface defect, structure, polycrystallinity, and arrangement of monolayers. In Table 5.3, it is also noted that the advancing contact angles for the annealed and non-annealed surfaces are nearly identical and did not change very much, for both ethylene glycol and hexadecane. However, the molecular interactions between hexadecane/$CH_3(CH_2)_{17}SH$ and ethylene glycol/$CH_3(CH_2)_{17}SH$ on two different Au surfaces are not clearly known. One may conclude that, whatever these interactions are, they appear to be insensitive to the structural changes and surface defects of the monolayers. Interpretation of such angles on the non-annealed ones would be difficult [116, 117, 118]. Since the annealed surfaces contain less defects, additional variation of the solid-liquid interfacial interactions $\Delta\gamma_{sl}$ would be minimal. Therefore, the surface structures of the underlying gold on which the monolayers of octadecanethiol are formed can affect directly the interpretation of contact angles. With the above stipulation, the variation of γ_{sl} as a result of surface structural change can be estimated if assuming γ_{sv} for the non-annealed and annealed Au to be the same. Therefore, a $\Delta\gamma_{sl}$ of 12.9 mJ/m^2 can be estimated by taking the difference in the water advancing angles, $\Delta\gamma_{sl} = [72.7\ (\cos 107° - \cos 118°)]$, using Young's equation. This value represents an increase in γ_{sl} due to the variation of surface structures of octadecanethiol SAM absorbed onto Au when interacting with water. However, conventional thinking would have interpreted the water contact angle of 118° for octadecanethiol SAM on Au to have a much lower solid surface tension similar to that of fluorocarbon [$\gamma_{sv} = \sim 12$ mJ/m^2], rather than a γ_{sv} of 19–20 mJ/m^2 for methyl-terminated surfaces.

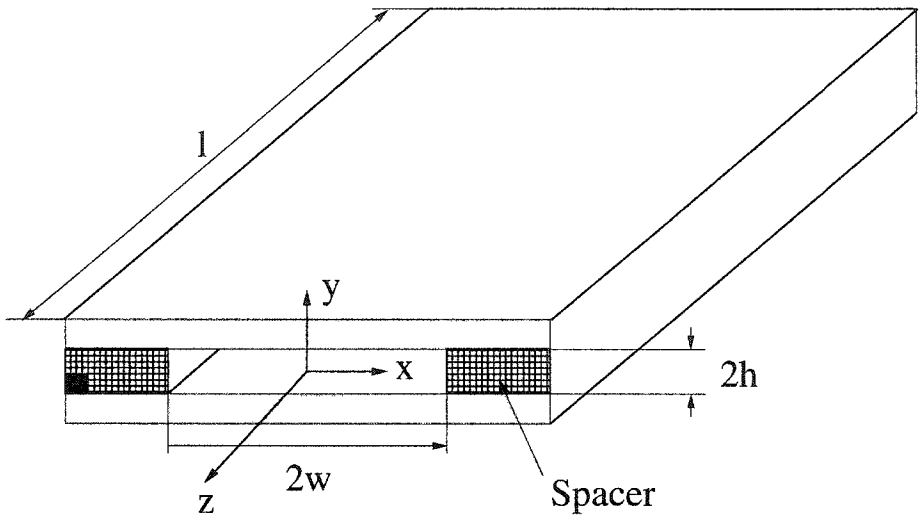

Figure 5.9: Illustration of the microchannel formed between two microscope slides

5.3 Experimental investigation of liquid slippage on SAMs

In the above section, the nano-structure of substrate has been shown to influence the formation of octadecanethiol SAM and hence the contact angle of water. In this section, the slippage of flow on SAMs coatings is investigated. Octadecanethiol SAMs on annealed and non-annealed gold substrates are used as hydrophobic coatings; while 16-Mercaptohexadecanoic acid $[HS(CH_2)_{15}CO_2H]$ SAM is used as hydrophilic coating.

In our experiments, it is assumed that if the liquid can wet lyophobic coating, it does not slip in microchannel with such coating. Vinogradova pointed out that the advancing contact angle $\theta_a \geq 70°$ is the threshold advancing contact angle of slippage [119]. Churaev *et al.* observed flow increase in capillaries with $\theta_a \geq 70°$, but not in capillaries with $\theta_a < 70°$ [52]. Here, ethanol is used as the wetting liquid. The liquid-vapor surface tension of ethanol γ_{lv} is 21.97 mJ/m^2. In last section, the solid-vapor surface tension of octadecanethiol SAM, γ_{sv}, is shown to be 20 mJ/m^2, which is the same as other methyl-terminated surfaces. In order to eliminate electroviscous effects, the two electrodes of the microchannel are always short-circuited for 0.01 M KCL solution.

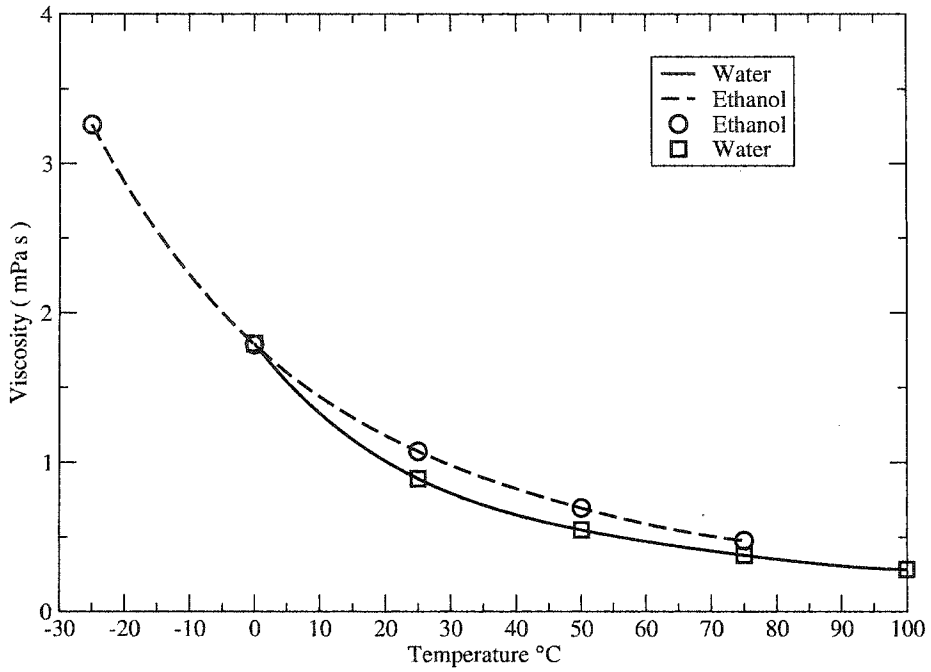

Figure 5.10: The viscosity of water and ethanol as a function of temperature

The microchannel has a rectangular cross section (see Fig. 5.9). Since $w \gg h$, the rectangular microchannel can be considered a parallel-plate microchannel. Without electroviscous effects, the flow rate of flow in parallel-plate microchannel is

$$q = \frac{1}{\mu}\left(-\frac{dp}{dz}\right)\left(\frac{2}{3}h^3 - 2\beta h^2\right) . \tag{5.1}$$

Because liquid viscosities change with temperature, the temperature in real time is recorded for corresponding viscosity at a given temperature. In Table 5.4, viscosities of ethanol and water are listed at different temperatures [120]. In Fig. 5.10, two functions of viscosities for water and ethanol, with respect to temperature, are obtained by fitting experimental data of Table 5.4 [121].

In actual experiment, the measured pressure drop is the total pressure drop, including pressure decay at the inlet and outlet [69, 10]. In the entrance region, the flow is not a fully developed laminar flow and the entrance region length l_{in} is given

Table 5.4: Viscosities of liquids

Temperature	Viscosity of water (mPa s)	Viscosity of ethanol (mPa s)
-25°		3.262
0°	1.793	1.786
25°	0.890	1.074
50°	0.547	0.694
75°	0.378	0.476
100°	0.282	

by [69, 10]

$$l_{in} = 0.02(2 * h)Re \quad , \quad Re = \frac{\rho_d v_m D_h}{\mu} \ , \tag{5.2}$$

where $D_h = 4hw/(h + w)$ is the hydraulic diameter of the rectangular microchannel 5.9, ρ_d is density and v_m is the mean velocity. In this region, the pressure drop is calculated by

$$\triangle p_{in} = \frac{k_{in}\rho_d l_{in}}{2D_h} v_m^2 \ , \tag{5.3}$$

where k_{in} is the friction coefficient given by [69, 10]

$$\triangle k_{in} = \frac{96}{Re} + \frac{1}{Re}\left[\frac{0.774}{l_{in}/4hRe} - \frac{0.00089}{(l_{in}/4hRe)^2}\right] \ , \tag{5.4}$$

At the exit of the flow, the cross section is greatly increased as the liquid leaves the parallel slit microchannel and the flow becomes turbulent. The pressure decay at the outlet is estimated by [69, 10]

$$\triangle p_{out} = \frac{\rho_d}{2} v_m^2 \ , \tag{5.5}$$

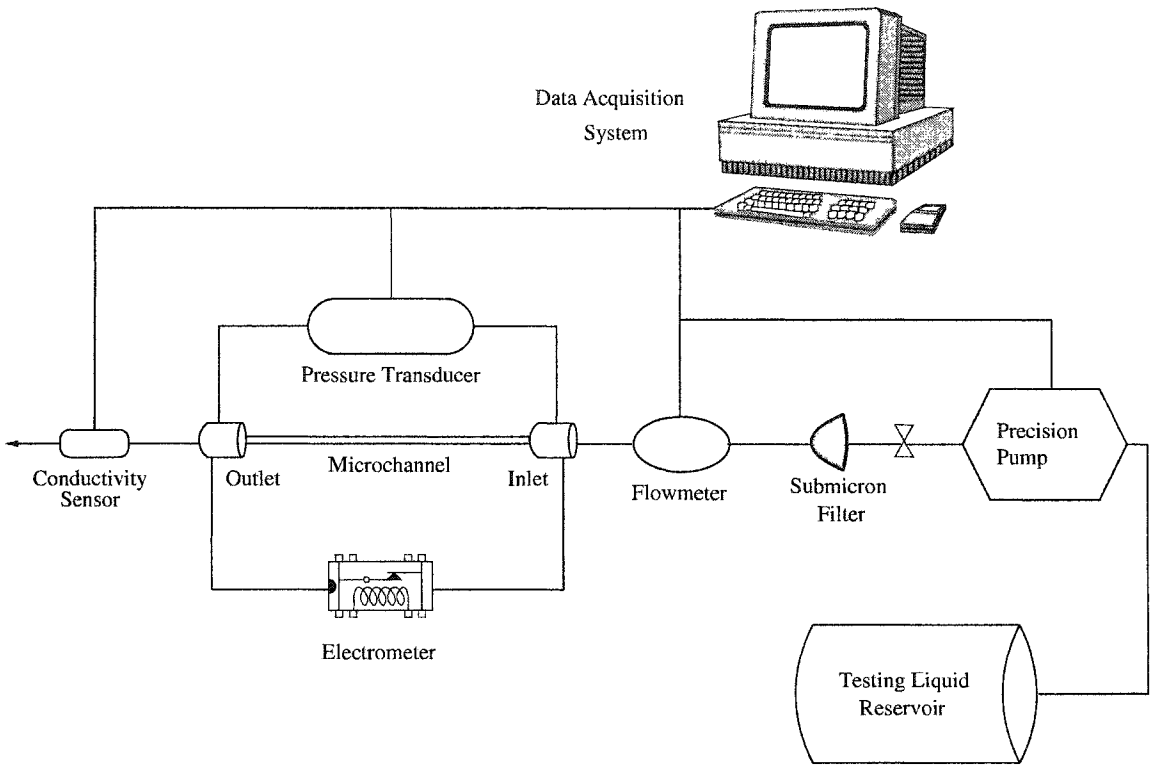

Figure 5.11: Schematic of the experimental system

Thus, the flow rate and the pressure gradient in Eq. 5.1 are

$$q = \frac{q_{measured}}{2w},$$
$$\frac{dp}{dz} = \frac{\triangle p_{measured} - \triangle p_{in} - \triangle p_{out}}{l - l_{in}}. \tag{5.6}$$

5.3.1 Experimental setup

The experimental system is shown in Fig. 5.11. The precision pump supplies different liquids to the flow section from the testing liquid reservoir. The flow section includes a submicron filter, a flow-meter, an electro-meter, a pressure transducer, microchannel, a data acquisition system and a conductivity sensor. Details of these equipment are listed in Table 5.5. The inlet and outlet of microchannel will make up of two sumps to hold probes of electro-meter and pressure transducer. All connection parts,

valves, and tubings are plastic or Teflon to minimize the influence for conductivity. A stopwatch is used to measure the time it takes for accumulation and the weight of the collected liquid can be measured by an electronic balance. Thus, the flow rate can be calculated by the weight, time and liquid density. This redundant procedure provides an additional check on the reading from the flow-meter and the precision pump. The tolerance of the flow rate provided by the precision pump is controlled within 1%.

Table 5.5: Equipments used for microchannel experimental setup.

Equipment	Supplier	Model #
Data acquisition system	Dycor	CIO-DAS08jr "Wizard" Software
Flow-meter	Thermal Instruments	600-9/316SS/h Tube Connection
Precision pump	ISCO	LC-5000
Pressure transducer	Omega	PX26-030DV CX136-4
Conductivity sensor	WJF instrumentation	HI 710m HI 7639
Multimeter	Hewlett-Packard	HP 3478A
Filter	Fisher Scientific	Anotop25 Polycap75

5.3.2 Experimental section

5.3.2.1 Materials

Microscope slides are 25 mm×75 mm×1 mm and were obtained from Fisher Scientific. Deionized ultrafiltered (DIUF) water was obtained from Fisher Scientific. Strips of a thin plastic shim were obtained from Small Parts Inc.. Octadecanethiol [$CH_3(CH_2)_{17}SH$], 16-mercaptohexadecanoic acid [$HS(CH_2)_{15}CO_2H$] and KCl were obtained from Aldrich. Ethanol (100%) was obtained from the Chemistry Dept. at the University of Alberta. Platinum electrodes were obtained from A-M Systems Inc.

and epoxy was obtained from Devcon.

5.3.2.2 Fabrication of microchannel

Microscope slides were firstly cut into the size of 25 mm×45 mm×1 mm. Supported gold films were prepared by sequentially evaporating titanium ($\sim$ 10 nm) and gold ($\sim$ 100 nm) onto the cut rectangular microscope slides in a diffusion-pumped vacuum chamber at $\sim 10^{-6}$ torr. The chamber was backfilled with air and the substrates were used within 48 h of preparation. The evaporated surfaces were rinsed with ethanol before SAMs formation. Octadecanethiol or 16-Mercaptohexadecanoic acid SAMs were prepared by immersing into 1 mM of $CH_3(CH_2)_{17}SH$ or 1 mM of $HS(CH_2)_{15}CO_2H$ in ethanol overnight. The resulting surfaces were rinsed with ethanol and blown dry by nitrogen before use. Some evaporated gold substrates were also flame annealed for $\sim$ 30 s using a bunsen burner under ambient laboratory condition. After $\sim$ 1 minute, the annealed substrate was then immersed into 1 mM of $CH_3(CH_2)_{17}SH$ in ethanol overnight.

After coating SAMs on microscope slides, to form a microchannel, two strips of a thin plastic shim were used as the spacer and put between a pair of silicon plates in the length direction along the sides of the plates, so that a flow passage of $2w$ width was formed. Then, a specially designed clapper, which can provide a constant torque, was used to fix the relative position of the plates and the thin spacers. Finally, epoxy resin was applied to bond the two microscope slides together and to seal all the openings except the inlet and outlet of the microchannel. The cross section of such a microchannel is illustrated in Fig. 5.9.

The width and length of the microchannel can be accurately measured by using a precision gauge. To determine the height of the microchannels was the biggest challenge. As optical microscopes do not provide the required resolution, the channel height was calibrated by an indirect method that involves the flow of a wetting liq-

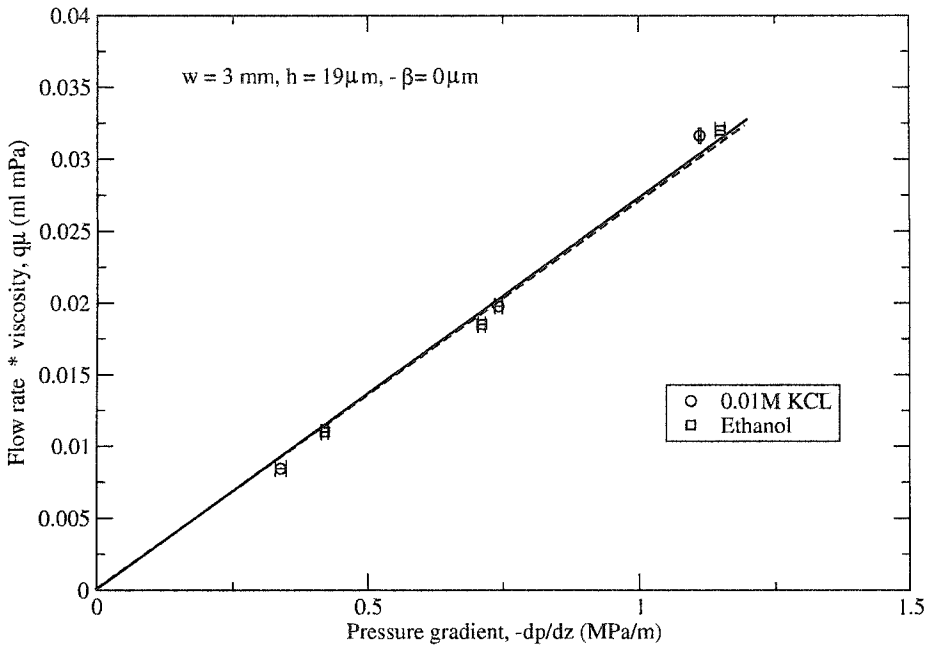

Figure 5.12: Experimental data of 0.01 M KCl and ethanol in -COOH microchannel

uid (ethanol) through the microchannel. To eliminate electroviscous effects, the two electrodes are short-circuited. The liquid flow in such a case is basically a Poiseuille laminar flow. Therefore, the channel height can be determined from the measured pressure drop and flow rate by using the Poiseuille flow equation [69].

5.3.2.3 Experimental procedures, results and discussion

In each measurement, the pump was set to maintain a constant flow rate. The flow was considered to have reached a steady state when the readings of the pressure drop remain constant. At such a steady state, temperature, flow rate and pressure drop were recorded. For a given channel and a given testing liquid, the measurements for all the parameters were repeated at least twice for the same flow rate. All data for a given channel were recorded in the same day. Measurements were also repeated on a different day and the results are reproducible.

The measured experimental data of 0.01 M KCl and ethanol in a -COOH mi-

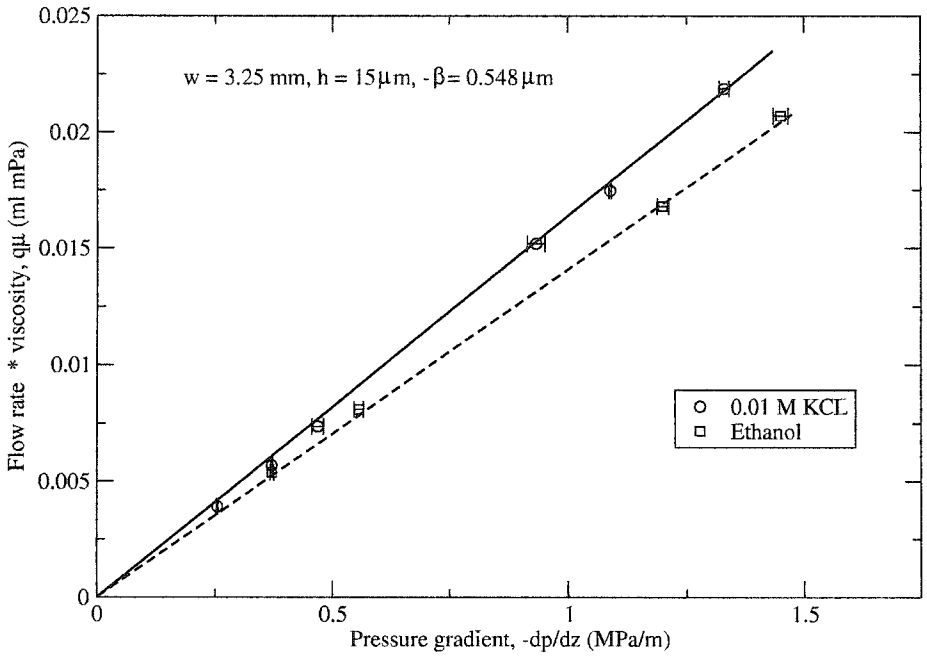

Figure 5.13: Experimental data of 0.01 M KCl and ethanol in -CH_3 microchannel with non-annealed gold

crochannel is shown in Fig. 5.12. The solid and dashed lines are fitted lines of the flow rate as a function of pressure gradient for 0.01 M KCl and ethanol, respectively. The solid line is nearly identical to the dashed one suggesting that no slip happens on the hydrophilic surface exposing -COOH function groups. The measured experimental data of 0.01 M KCl and ethanol in microchannel with octadecanethiol [$CH_3(CH_2)_{17}SH$] coated on non-annealed gold is shown in Fig. 5.13. From the experimental data, the calculated slip length is 0.548 μm, which is the same order of other experimental results [48, 122, 54]. The measured experimental data of the same liquids in microchannel with octadecanethiol [$CH_3(CH_2)_{17}SH$] coated on annealed gold is shown in Fig. 5.14. From the experimental data, the calculated slip length is 0.318 μm, which is smaller than that of the microchannel with octadecanethiol [$CH_3(CH_2)_{17}SH$] coated on non-annealed gold. These results relate quantitatively with the contact angle measurements in Section 5.2.

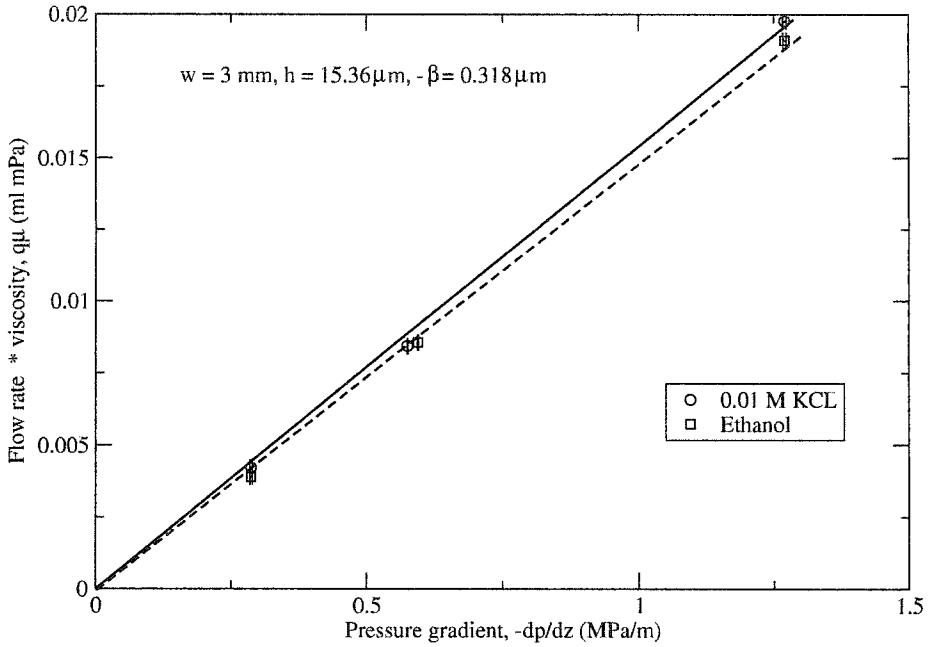

Figure 5.14: Experimental data of 0.01 M KCl and ethanol in -CH_3 microchannel with annealed gold

5.4 Conclusions

In this chapter, the effects of nano-crystalline on hydrophobicity of SAMs are studied. The slippage of flow on hydrophobic surfaces are experimentally observed. Formation of SAMs affects contact angle phenomena of water, so as to the flow behavior of water flow. The slip length of octadecanethiol SAMs on annealed gold is larger than that of on non-annealed gold, in good agreement with that shown in contact angles of water.

Chapter 6

Summary and Future Work

6.1 Summary

Solid-liquid interfacial effect on pressure-driven liquid flow in microchannels has been studied in this thesis. Two kinds of surface effects were considered: electrokinetic and hydrophobicity effects. On electrokinetic side, pressure-driven electrokinetic flow in parallel-plate microchannels and porous media were studied. The effects of flow field on the electric double layer distribution for a dilute electrolyte (DIUF water) in a streaming potential mode have been demonstrated numerically and experimentally for a 40 μm parallel-plate microchannel. The effects of flow-induced electrical field on the electric double layer have been studied for different pore sizes media. Regarding hydrophobicity effect, a promising slip coating SAMs is proposed. The research of surface effect on pressure-driven liquid flow are summarized below:

1. numerical simulation on pressure-driven electrokinetic flow in parallel-plate microchannels is performed. In the simulation, a more general model other than Poisson-Boltzmann equation is employed.

2. The potential distribution of pressure-driven flow in parallel-plate microchannels was studied experimentally.

3. The pressure-driven electrokinetic flow with an external load in porous media is studied theoretically and experimentally.

4. An electrokinetic generator consisting of porous media has been proposed.

5. A promising slip coating SAMs was proposed and the slip lengths for liquid flow in microchannels were determined experimentally.

6.2 Future work

The following work will benefit future research in the area:

1. To build a new model by employing the convection-diffusion-migration equation for simulation of electrokinetic flow in porous media.

2. To investigate the role of surface conductance in microfluidics and nanofluidics.

3. To improve the efficiency of EK generation by employing different solid materials and working liquids.

4. To find the quantitative relation between slip length and wettability based on a deeper understanding of solid-liquid interactions.

BIBLIOGRAPHY

[1] C. M. Ho and Y. C. Tai. *Annu. Rev. Fluid Mech.*, 30:579–612, 1998.

[2] D. R. Crow. *Principles and Applications of Electrochemistry.* Chapman and Hall Chemistry Textbook Series. Great Britain, second edition, 1979.

[3] H. Helmholtz. *Wied. Ann.*, 7:337, 1879.

[4] G. Gouy. *J. phys.*, 9:457, 1910.

[5] D. L. Chapman. *Phil. Mag.*, 25:475, 1913.

[6] A. J. Bard and L. R. Faulkner. *Electrochemical Methods Fundamentals and Applications.* John Wiley & Sons, New York.

[7] R. J. Hunter. *Zeta potential in Colloid Science, Principals and Applications.* Academic Press, New York, 1981.

[8] J. Lyklema. *Fundamentals of Interface and Colloid Science*, volume II. Academic Press, 1995.

[9] F. Urban, H. L. White, and E. A. Strassner. *J. Phys. Chem.*, 39:311, 1935.

[10] C. Werner, H. Körber, R. Zimmermann, S. Dukhin, and H.-J. Jacobasch. *J. Colloid Interface Sci.*, 208:329–346, 1998.

[11] G. Jones and L. Wood. *J. Chem. Phys.*, 13:106, 1945.

[12] H. B. Bull. *J. Phys. Chem.*, 39:577, 1935.

[13] H. J. Jacobasch. *Acta Polym.*, 31:481, 1980.

[14] R. S. Sanders, R. S. Chow, and J. H. Masliyah. *J. Colloid interface Sci.*, 174:230, 1995.

[15] D. R. Briggs. *J. Am. Chem. Soc.*, 50:2358, 1928.

[16] H. L. White, F. Urban, and E. T. Krick. *J. Phys. Chem.*, 36:120, 1932.

[17] D. Erickson, D. Li, and C. Werner. *J. Colloid Interface Sci.*, 232:186–197, 2000.

[18] R. J. Hunter. *Introduction to Modern Colloid Science.* Oxford University Press Inc., 1993.

[19] G. Quinke. *Pogg. Ann. Physik.*, 107:1, 1859.

[20] P. Debye and E. Hückel. *Phys. Z.*, 24:185, 1923.

[21] O. Stern. *Z. Elektrochem.*, 30:508, 1924.

[22] M. Smoluchowski. *Krak. Anz.*, page 182, 1903.

[23] D. Burgreen and F. R. Nakache. *J. Phys. Chem.*, 68:1084, 1964.

[24] C. L. Rice and R. Whitehead. *J. Phys. Chem.*, 69:4017–4024, 1965.

[25] S. Levine, J. R. Marriott, G. Neale, and N. Epstein. *J. Colloid Interface Sci.*, 52:136–149, 1975.

[26] J. T. G. Overbeek. *Colloid Science.* Elsevier Amsterdam, 1952.

[27] E. González-Tovar, M. Lozada-Cassou, and W. Olivares. *J. Chem. Phys.*, 94:2219, 1991.

[28] W. Olivares, B. Sulbarán, and M. Lozada-Cassou. *J. Phys. Chem.*, 97:4780, 1993.

[29] W. Olivares, B. Sulbarán, and M. Lozada-Cassou. *J. Chem. Phys.*, 103:8179, 1995.

[30] H. Freundlich and G. Ettisch. *Z. physik. Chem.*, 116:401, 1925.

[31] D. R. Briggs. *J. Am. Chem. Soc.*, 50(9):2358, 1956.

[32] D. R. Briggs. *J. Phys. Chem.*, 32:641, 1928.

[33] D. W. Fuerstenau. *J. Phys. Chem.*, 60(7):981, 1956.

[34] M. Zembala and Z. Adamczyk. *Langmuir*, 16(4):1593, 2000.

[35] H. B. Bull and R. A. Gortner. *J. Phys. Chem.*, 32:111, 1932.

[36] E. A. Van Atta H. L. White, F. Urban. *J. Phys. Chem.*, 36:3152, 1932.

[37] A. Rutgers and M. de Smet. *Trans. Faraday Soc.*, 41:758, 1945.

[38] R. Dubois and A. H. Roberts. *J. Phys. Chem.*, 40:543, 1936.

[39] L. S. Moyer and H. A. Abramson. *J. Gen. Physiol.*, 19:727, 1936.

[40] K. Kanamaru. *Chem. Abstracts*, 25:3895, 1931.

[41] K. J. Kim, A. G. Fane, M. Nystrom, A. Pihlajamaki, W. R. Bowen, and H. Mukhtar. *Journal of Membrane Science*, 116:149–159, 1996.

[42] C. Werner, R. Zimmermann, and T. Kratzmüller. *Colloids and surfaces A*, 192:205–213, 2001.

[43] R. Schweiss, C. Welzel, P. B.and Werner, and W. Knoll. *Langmuir*, 17:4304–4311, 2001.

[44] R. Schweiss, P.B. Welzel, C. Werner, and W. Knoll. *Colloids Surface A. Physiochem. Eng. Aspects*, 195:97, 2001.

[45] Y. M. Chan, R. Schweiss, C. Werner, and M. Grunze. *Langmuir*, 19:7380–7385, 2003.

[46] R.-J.Yang, L.-M.Fu, and C.-C.Hwang. *J. Colloid Interface Sci.*, 244:173–179, 2001.

[47] A. van Theemsche, J. Deconinck, B. V. D Bossche, and L. Bortels. *Anal. Chem.*, 74:4919, 2002.

[48] D. C. Tretheway and C. D. Meinhart. *Phys. Fluid*, 14:L9–L12, March 2002.

[49] R. Pit, H. Hervet, and L. Léger. *Phys. Rev. Lett.*, 85(5), July 2000.

[50] C. Cottin-Bizonne, S. Jurine, J. Baudry, J. Crassous, F. Restagno, and É. Charlaix. *Eur. Phys. J. E.*, 9:47–53, 2002.

[51] E. Schnell. *J. Appl. Phys.*, 27:1149–1152, 1956.

[52] N. V. Churaev, V. D. Sobolev, and A. N. Somov. *J. Colloid Interface Sci.*, 97:574, 1984.

[53] K. Watanabe, Y. Udagawa, and H. Udagawa. *J. Fluid Mech.*, 381:225–238, 1999.

[54] Y. X. Zhu and S. Granick. *Phys. Rev. Lett.*, 87(9):980, 2001.

[55] J. T. Cheng and N. Giordano. *Phys. Rev. E*, 65:031206, 2002.

[56] P. A. Thompson and S. M. Troian. *Nature*, 389:360–362, September 1997.

[57] J. L. Barrat and L. Bocquet. *Phys. Rev. Lett.*, 82:4671, 1999.

[58] J. L. Barrat and L. Bocquet. *Faraday Discuss*, 112:119, 1999.

[59] A. Szymczyk, P. Fievet, M. Mullet, J. C. Reggiani, and J. Pagetti. *J. of Membrane Science*, 143:189–195, 1998.

[60] N. A. Patanka and H. Hu. *Anal. Chem.*, 70:1870, 1998.

[61] L. Hu, J. D. Harrison, and J. H. Masliyah. *J. Colloid Interface Sci.*, 215:300–312, 1999.

[62] S. V. Ermakov, S. C. Jacobson, and J. M. Ramsey. *Anal. Chem.*, 70:4494, 1998.

[63] M. J. Mitchell, R. Qiao, and N. R. Aluru. *J. Microelectromech. Sys.*, 9:435, 2000.

[64] J. M. MacInnes. *Chem. Eng. Sci.*, 57:4539, 2002.

[65] J. Yang, J. H. Masliyah, and D. Y. Kwok. *Langmuir*, 20:3862–3871, 2004.

[66] Y. Nakayama and R. F. Boucher. *Introduction to Fluid Mechanics.* John Wiley & Sons, New York.

[67] Lloyd A. Wood. *J. Am. Chem. Soc.*, 68:432–437, 1946.

[68] P. Attard, D. Antelmi, and I. Larson. *Langmuir*, 16:1542, 2000.

[69] L. Q. Ren, D. Li, and W. L. Qu. *J. Colloid Interface Sci.*, 233:12–22, 2001.

[70] Y. Gu and D. Li. *J. Colloid Interface Sci.*, 226:328, 2000.

[71] S. Levine, J. R. Marriott, and K. Robinson. *J. Chem. Soc. Faraday Trans. II*, 71:1–11, 1975.

[72] J. F. Osterle. *J. Appl. Mech.*, 31:161, 1964.

[73] A. J. Kuin and H. N. Stein. *J. Colloid Interface Sci.*, 108:377, 1985.

[74] R. W. O'Brien and W. T. Perrins. *J. Colloid Interface Sci.*, 99:20, 1984.

[75] R. W. O'Brien. *J. Colloid Interface Sci.*, 110:477, 1986.

[76] R. Midmore and R. W. O'Brien. *J. Colloid Interface Sci.*, 123:486, 1988.

[77] J. H. Masliyah. *Electrokinetic Transport Phenomena.* Alberta Oil Sands Technology and Research Authority, 1994.

[78] A. Shadowitz. *The Electromagnetic Field.* Dover, 1975.

[79] J. Lyklema and M. Minor. *Colloids and Surfaces A*, 140:33–41, 1998.

[80] R. Wasche, M. Naito, and V. A. Hackley. *Powder Technology*, 123:275–281, 2002.

[81] G. M. Mala, D. Li, and J. D. Dale. *Int. J. Heat Mass Transfer*, 40:3079–3088, 1997.

[82] G. M. Mala, D. Li, C. Werner, H. J. Jacobasch, and Y. B. Ning. *Int. J. Heat Liquid Flow*, 18:489–496, 1997.

[83] J. Yang and D. Y. Kwok. *Langmuir*, 19:1047–1053, 2003.

[84] J. Yang and D. Y. Kwok. *J. Micromech. Microeng.*, 13:115–123, 2003.

[85] J. Yang and D. Y. Kwok. *J. Chem. Phys.*, 118:354–363, 2003.

[86] J. Yang and D. Y. Kwok. *J. Phys. Chem. B*, 106:12851–12855, 2002.

[87] B. Li and D. Y. Kwok. *Phys. Rev. Lett.*, 19:12450, 2003.

[88] B. Li and D. Y. Kwok. *Langmuir*, 19:3041–3048, 2003.

[89] C. D. Bain and G. M. Whitesides. *Angew. Chem. Int. Ed.*, 28(4):506, 1989.

[90] G. M. Whitesides and P. E. Laibinis. *Langmuir*, 6:87, 1990.

[91] A. Ulman. *Introduction to Thin Organic Films: From Langmuir-Blodgett to Self-Assembly.* Academic Press, Boston, 1991.

[92] L. H. Dubois and R. G. Nuzzo. *Ann. Rev. Mater. Sci.*, 43:437, 1992.

[93] Y. Xia and G. M. Whitesides. *Angew. Chem. Int. Ed.*, 37:550, 1998.

[94] W. C. Bigelow, D. L. Pickett, and W. A. Zisman. *J. Colloid Interface*, page 513, 1946.

[95] R. L. Shuler and W. A. Zisman. *J. Phys. Chem.*, pages 1397–1405, 1975.

[96] M. K. Bernett and W. A. Zisman. *Adv. Chem. Ser.*, 8:199–211, 1975.

[97] R. G. Nuzzo, F. A. Fusco, and D. L. Allara. *J. Am. Chem. Soc.*, 109:2358–2368, 1987.

[98] D. Y. Kwok, H. Ng, and A. W. Neumann. *J. Colloid Interface Sci.*, 225(2):323, 2000.

[99] Y. Rotenberg, L. Boruvka, and A. W. Neumann. *J. Colloid Interface Sci.*, 93:169, 1983.

[100] P. Cheng, D. Li, L. Boruvka, Y. Rotenberg, and A. W. Neumann. *Colloids Surfaces*, 43:151, 1990.

[101] D. Y. Kwok, R. Lin, M. Mui, and A. W. Neumann. *Colloids Surfaces A: Physicochem. Eng. Aspects*, 116:63, 1996.

[102] D. Y. Kwok, T. Gietzelt, K. Grundke, H. J. Jacobasch, and A. W. Neumann. *Langmuir*, 13:2880, 1997.

[103] S. Lahooti, O. I. del Río, P. Cheng, and A. W. Neumann. Axisymmetric drop shape analysis. In J. K. Spelt and A. W. Neumann, editors, *Applied Surface Thermodynamics*, pages 441–507. Marcel Dekker Inc., New York, 1996.

[104] D. Y. Kwok, A. Leung, C. N. C. Lam, A. Li, R. Wu, and A. W. Neumann. *J. Colloid Interface Sci.*, 206:44, 1998.

[105] D. Y. Kwok, A. Leung, A. Li, C. N. C. Lam, R. Wu, and A. W. Neumann. *Colloid Polym. Sci.*, 276:459, 1998.

[106] D. Y. Kwok, C. J. Budziak, and A. W. Neumann. *J. Colloid Interface Sci.*, 173:143, 1995.

[107] P. E. Lai106binis, G. M. Whitesides, D. L. Allara, Y. T. Tao, A. N. Parikh, and R. G. Nuzzo. *J. Am. Chem. Soc.*, 113:7152, 1991.

[108] P. E. Laibinis, R. G. Nuzzo, and G. M. Whitesides. *J. Phys. Chem.*, 96:5097, 1992.

[109] A. W. Neumann. *Adv. Colloid Interface Sci.*, 4:105, 1974.

[110] W. Guo and G. K. Jennings. *Langmuir*, 18:3123, 2002.

[111] W. Haiss, D. Lackey, J. K. Sass, and K. H. Bescoke. *J. Chem. Phys.*, 95:2193, 1991.

[112] E. Delamarche, B. Michel, H. Kang, and Ch. Gerber. *Langmuir*, 10:4103, 1994.

[113] Y. S. Shon and T. R. Lee. *Langmuir*, 15:1136, 1999.

[114] D. J. Vanderah, C. W. Meuse, V. Silin, and A. L. Plant. *Langmuir*, 14:6916, 1998.

[115] R. D. Weinstein, D. Yan, and G. K. Jennings. *Ind. Eng. Chem. Res.*, 40:2046, 2001.

[116] J. Drelich and J. D. Miller. *J. Colloid Interface Sci.*, 167:217, 1994.

[117] A. Amirfazli, D. Y. Kwok, J. Gaydos, and A. W. Neumann. *J. Colloid Interface Sci.*, 205:1, 1998.

[118] J. Drelich, J. L. Wilbur, J. D. Miller, and G. M. Whitesides. *Langmuir*, 12:1913, 1996.

[119] O. I. Vinogradova. *Int. J. Miner. Process.*, 56:31–60, 1999.

[120] D. R. Lide, editor. *CRC handbook of chemistry and physics.* Cleveland : Chemical Rubber Pub. Co., 82nd edition, 2001/2002.

[121] E. Hatschek. *The viscosity of liquids.* London, G. Bell and sons, ltd., 1928.

[122] N. V. Churaev, V. D. Sobolev, and A. N. Somov. *J. Colloid Interface Sci.*, 97:574, 1998.